Adjustable-Delay RIS is Capable of Improving OFDM Systems

Jiancheng An, *Member, IEEE*, Chao Xu, *Senior Member, IEEE*, Derrick Wing Kwan Ng, *Fellow, IEEE*, Chau Yuen, *Fellow, IEEE*, and Lajos Hanzo, *Life Fellow, IEEE*

***Abstract*—Reconfigurable intelligent surfaces (RIS) demonstrate the potential to improve the spectrum and energy efficiency of wireless networks. In this paper, we investigate multiple-RIS-assisted orthogonal frequency division multiplexing (OFDM) communications. Specifically, we generalize the existing RIS concept conceived for frequency-flat channels to the adjustable-delay RIS by introducing varactor diodes. In contrast to conventional reflecting elements, each adjustable-delay RIS element is capable of storing and retrieving the impinging electromagnetic waves upon dynamically controlling its electromagnetically induced transparency (EIT), thus imposing an extra delay onto the incident signals. This allows for aligning multiple signal copies via multiple RISs. To this end, we formulate a rate-maximization problem by jointly optimizing the transmit power allocation and the RIS reflection coefficients as well as the RIS delays. To address the coupling issue between these optimization variables, we propose a computationally efficient algorithm to find a high-quality solution to the non-convex design problem by alternately optimizing the transmit power allocation and the RIS reflection pattern, including both the reflection coefficients and the delays. Furthermore, we conceive a low-complexity reflection optimization scheme upon aligning the strongest taps of all reflected channels, while ensuring that the maximum delay spread introduced by extra RIS delays does not exceed the length of the cyclic prefix. Our simulation results demonstrate that the proposed design significantly improves the achievable rate as well as the RIS's adaptability to wideband signals compared to various benchmark schemes operating without adjustable-delay RIS. Moreover, it is shown that there exists a fundamental trade-off between the adjustable delay margin to align different reflected channels and the practical component's power decay caused by delay.**

***Index Terms*—Reconfigurable intelligent surface (RIS), orthogonal frequency division multiplexing (OFDM), reflection pattern optimization, power allocation, adjustable-delay metasurface.**

This research is supported by the Ministry of Education, Singapore, under its MOE Tier 2 (Award number MOE-T2EP50220-0019) and Science and Engineering Research Council of A*STAR (Agency for Science, Technology and Research) Singapore, under Grant No. M22L1b0110. D. W. K. Ng is supported by the Australian Research Council's Discovery Projects (DP230100603). L. Hanzo would like to acknowledge the financial support of the Engineering and Physical Sciences Research Council projects EP/W016605/1, EP/X01228X/1 and EP/Y026721/1 as well as of the European Research Council's Advanced Fellow Grant QuantCom (Grant No. 789028). *(Corresponding author: Chau Yuen.)*

J. An and C. Yuen are with the School of Electrical and Electronics Engineering, Nanyang Technological University, Singapore 639798 (e-mail: jiancheng.an@ntu.edu.sg; chau.yuen@ntu.edu.sg).

C. Xu and L. Hanzo are with the School of Electronics and Computer Science, University of Southampton, Southampton SO17 1BJ, U.K. (e-mail: cx1g08@soton.ac.uk; lh@ecs.soton.ac.uk).

D. W. K. Ng is with the School of Electrical Engineering and Telecommunications, University of New South Wales, Sydney, NSW 2052, Australia (e-mail: w.k.ng@unsw.edu.au).

I. Introduction

THE explosive growth of mobile data traffic has continuously driven innovation in wireless communication technologies, which has led to massive multiple-input multiple-output (MIMO) schemes [1], millimeter wave (mmWave) communications [2], and heterogeneous networks (HetNet) [3], as well as advances in channel coding design [4]. Looking ahead to 2030 and beyond, the sixth-generation (6G) mobile networks are expected to provide dramatically higher network capacity (Terabits/second) to cope with the escalating connection density (10^7 devices/km^2), while reducing latency to sub-millisecond levels [5]. While massive MIMO and mmWave communications achieve dramatic spectral efficiency improvements, the deployment of large-scale antenna arrays and the ever-increasing bandwidth generally result in higher implementation costs and increased power consumption [6]. Additionally, it will be challenging to meet the ambitious communication goals hypothesized in the 6G vision, such as increased network energy efficiency, near 100% coverage, support for high mobility, and intelligent resource allocation purely relying on existing communication technologies [7]. As a result, developing green communications and seamless connectivity for 6G mobile networks remains crucial [8].

Recently, reconfigurable intelligent surfaces (RIS) and their various relatives have been proposed for achieving the aforementioned goals [9]–[12]. Specifically, RIS is a programmable metasurface comprised of a large number of passive reflecting elements, each of which can induce an adjustable phase shift and/or an attenuation for the incident signals, allowing to customize a favorable wireless propagation environment according to the specific quality-of-service (QoS) requirements [13], [14]. By appropriately adjusting the phase shifts and attenuations caused by the RIS elements, the reflected signals can be constructively superimposed with those from other paths at the desired receivers for enhancing the received signal power and/or for suppressing the co-channel interference, both leading to improved wireless link performance [10], [15]. A RIS achieves higher energy efficiency in a full-duplex (FD) manner compared to the traditional amplify-and-forward/decode-and-forward relays, without incurring severe self-interference problems [9], [16]–[18].

In RIS-assisted wireless systems, channel state information (CSI) acquisition and reflection pattern optimization constitute a pair of fundamental problems [30]–[38]. For a completely

TABLE I
A COMPARISON OF OUR CONTRIBUTIONS TO EXISTING WORK.

Schemes	MIMO Setup	Optimization Objective	Frequency-Selective	Multiple RISs	RIS		
					Attenuation	Phase Shift	Delay
Huang *et al.* [15]	Multi-user MISO	Energy efficiency/Sum-rate				Continuous	
Wu *et al.* [10]	Multi-user MISO	Transmit power				Continuous	
An *et al.* [19]	Single-user MIMO	Channel capacity				Discrete	
Han *et al.* [20]	Single-user MISO	Ergodic spectral efficiency				Continuous	
Cui *et al.* [21]	Single-user MISO	Secrecy rate				Continuous	
Pan *et al.* [22]	Multi-cell multi-user MIMO	Weighted sum-rate				Continuous	
Guo *et al.* [23]	Multi-user MISO	Weighted sum-rate				Continuous	
Zhang *et al.* [24]	Single-user MIMO	Channel capacity	✓			Continuous	
Di *et al.* [25]	Multi-user MISO	Sum-rate			✓	Discrete	
Abeywickrama *et al.* [26]	Multi-user MISO	Transmit power			Coupled		
Yang *et al.* [27]	Single-user SISO	Achievable rate	✓		✓	Continuous	
Zheng *et al.* [28]	Single-user SISO	Achievable rate	✓			Continuous	
Han *et al.* [29]	Single-user SISO	Received SNR		✓		Continuous	
Our design	Single-user SISO	Achievable rate	✓	✓		Continuous	✓

passive RIS operating without any active wireless transceivers, it is a big challenge to separately estimate the individual channels of the base station (BS)-RIS and RIS-user equipment (UE) links. In order to address this issue, the authors of [33]–[36] proposed sophisticated methods for estimating the cascaded BS-RIS-UE channels. Based on the estimated CSI, the reflection pattern optimization is then performed jointly with other design parameters in conjunction with various optimization objectives, such as optimizing the power allocation of the zero-forcing (ZF) transmit precoding matrix for maximizing the energy efficiency [15], optimizing the transmit beamforming vectors for minimizing the transmit power [10], [19], optimizing the transmit beamforming vectors for maximizing the secrecy rate [21], [39], and optimizing the transmit precoding matrices of multiple BSs for maximizing the weighted sum rate [22], [40]. Moreover, in [20], [41], only the statistical CSI is required for optimizing the reflection pattern, since a large-scale reflection array generally results in a deterministic performance limit. More recently, a novel codebook-based solution was proposed to strike flexible trade-offs between the achievable rate and the pilot overhead [9], [42], [43]. Additionally, the RIS reflection coefficient optimization has also been combined with other potential technologies, such as physical layer security [44], unmanned aerial vehicles [45], mobile edge computing [46], holographic MIMO [47], [48], and may be carried out employing machine learning techniques [41], [49].

Nevertheless, it is worth noting that the prior works on RIS-aided wireless systems have mostly considered frequency-flat fading channels, where the RIS reflection coefficients are designed to align the phases of the reflected BS-RIS-UE links with that of the direct BS-UE link for coherent superposition. However, when frequency-selective fading channels are considered, the RIS reflection coefficients are required to cater for all subcarriers, making the underlying optimization problem more challenging to solve compared to its narrowband counterpart. To address this challenge, the authors of [27], [28], [50], [51] studied RIS-aided orthogonal frequency division multiplexing (OFDM) communications under frequency-selective channels. Specifically, to reduce the channel estimation overhead, *Yang et al.* [27] proposed a practical OFDM transmission protocol by grouping adjacent RIS elements together and only estimating the combined channel of each group. Based on this, they formulated a rate maximization problem by jointly optimizing the transmit power allocation and RIS reflection coefficients. An alternating optimization (AO) method relying on successive convex approximation was developed to obtain a high-quality suboptimal solution. Moreover, to reduce the implementation complexity, *Zheng and Zhang* [28] proposed a heuristic algorithm to optimize the RIS reflection coefficients by aligning the tap having the highest combined channel gain in the delay domain. More recently, *Zhang and Dai* [52] improved the capacity of wideband RIS-aided cell-free networks by replacing some of the BSs with energy-efficient RISs. In [53], the authors proposed an iterative majorization-minimization approach to optimize the RIS-based passive beamformer to maximize the total data rate across all subcarrier frequencies. **However, the strongest tap of different reflected channels may have different time delays, which limits the performance gains of RIS-assisted OFDM communications, especially in distributed RIS deployments.**

Against this background, in this paper, we investigate RIS-aided OFDM communications over frequency-selective channels. In particular, we first introduce the adjustable-delay RIS, which is capable of adjusting the delays of signals reflected by different RIS elements [54]–[56]. Fig. 1(a) illustrates a specific meta-atom that exhibits electromagnetically induced transparency (EIT), where the directions of the magnetic field (**B**) and electric field (**E**) of the incident waves are also displayed. Specifically, the meta-atom structure is made of copper and built on a dielectric substrate. Two varactor diodes, whose capacitance varies with the voltage across their surface, are inserted in opposite directions along the two side circuit paths. The meta-atom supports three resonant modes: a radiative mode, a trapped mode, and a control mode. Figs. 1(b)–(d) illustrate the current

flow for these three modes using dashed lines. The control mode occurs when only the control waves generated by a local oscillator are present[1]. Furthermore, in the absence of the control wave, the probe wave experiences high radiation loss in the radiative mode. However, after reintroducing the control wave and mixing it with the probe wave, other frequency components are produced via three-wave mixing in the nonlinear capacitors. This allows some probe-wave signals to be efficiently transmitted through the meta-atom. In this case, the RIS is switched from the radiative mode directly to the trapped mode. Therefore, given this circuit configuration, the incident signals can be stored for a while, matching the periods in the absence of the control wave. The accurate delay control can be realized using pulse width modulation signaling. Based on this model, we then develop an associated rate-maximization problem by jointly optimizing the power allocation and RIS reflection coefficients as well as RIS delays. The new delay DoF facilitates the alignment of the strongest taps of different reflected channels, thus improving the superimposed channel response in the frequency domain and resulting in an increased achievable rate. For the sake of illustration, we boldly and explicitly contrast our contributions to the existing works in Table I. Explicitly, the main contributions of this paper are summarized as follows:

1) We introduce a novel adjustable-delay RIS fabricated with varactor diodes [54], [55]. In contrast to the existing adjustable-phase meta-atom relying on PIN diodes, each adjustable-delay RIS element is capable of storing and retrieving the incident electromagnetic (EM) waves. Upon dynamically controlling its EIT properties, i.e., the ON/OFF state of the control waves, each meta-atom in Fig. 1(a) can adjust the storage time of the impinging waves, thus imposing an extra delay onto the incident signals.
2) We formulate an optimization problem aiming for maximizing the achievable rate by jointly optimizing the power allocation at the transmitter and the reflection coefficients as well as the delays at the RIS. Nevertheless, the problem formulated is non-convex and therefore non-trivial to solve optimally. To address this, we conceive an iterative algorithm that alternately optimizes the transmit power allocation and the RIS reflection pattern, including both the reflection coefficients and the delays.
3) In order to circumvent the high complexity of optimizing the RIS reflection coefficients, we propose a low-complexity scheme for aligning the strongest taps of all reflected channels in the delay domain, while ensuring that the maximum delay spread after adding extra RIS delays does not exceed the length of the cyclic prefix (CP).
4) Our numerical simulations evaluate the performance of the proposed designs. It is shown that the proposed design reduces to the conventional one when considering a single RIS. By contrast, when multiple RISs are deployed, jointly optimizing the reflection phase shifts and delays at the RIS achieves a higher rate than the systems operating without adjustable-delay RIS, for both perfect and estimated CSI scenarios. Additionally, considering the practical power loss of the adjustable-delay RIS component, it is unveiled that there generally exists a fundamental trade-off between the adjustable delay and the resultant power decay that maximizes the achievable rate.

[1]Note that introducing control waves requires additional hardware costs and energy consumption. However, a self-sustainable RIS with energy harvesting capabilities could help address these new challenges [57]. Additionally, the stored incident signals could potentially be transformed into energy for power supply [58]. In this paper, we focus on characterizing the performance limits provided by the additional delay degrees-of-freedom (DoF) of the RIS. Analyzing the fundamental tradeoffs between the performance improvements and the increased hardware costs is beyond the scope of this paper and is reserved for our future research.

The remainder of this paper is organized as follows. Section II introduces the model of adjustable-delay RIS-aided OFDM systems. Section III formulates the joint optimization problem of the transmit power allocation and the RIS reflection pattern for maximizing the achievable rate. Furthermore, in Section IV, we propose an AO algorithm for finding a near-optimal solution, while in Section V, we conceive a low-complexity method and analyze the theoretical performance. Section VI provides numerical simulations to characterize the performance of the proposed designs. Finally, Section VII concludes the paper.

Notations: Column vectors/matrices are denoted by boldface lowercase/uppercase letters, while sets are indicated with uppercase calligraphic letters; For a matrix $\mathbf{M}$ of arbitrary size, $\mathbf{M}^T$, $\mathbf{M}^*$, and $\mathbf{M}^H$ represent its transpose, conjugate and Hermitian transpose, respectively; $\mathrm{rank}\,(\mathbf{M})$ returns the rank of matrix $\mathbf{M}$; while $\mathrm{tr}\,(\mathbf{V})$ represents the trace of the square matrix $\mathbf{V}$; $\mathbf{0}_{x\times y}$ denotes an all-zero matrix of size $x \times y$; while $\mathbf{1}_{x\times y}$ denotes an all-one matrix of size $x \times y$; $\mathbf{I}_M$ represents the identity matrix of size M, while $\mathbf{e}_m$ denotes the m-th column of $\mathbf{I}_M$. Moreover, $\mathrm{diag}\,(\mathbf{v})$ denotes a diagonal matrix with the elements of $\mathbf{v}$ on its main diagonal and $\mathrm{diag}\,(\mathbf{V})$ represents a column vector formed by the main diagonals of the square matrix $\mathbf{V}$; $\|\mathbf{v}\|$ represents the Euclidean norm of vector $\mathbf{v}$; $|v|$ and $\angle v$ denote the modulus and the angle of a complex number v, respectively; while $\lfloor a \rceil$ represents the integer nearest to the real number a; $\otimes$ denotes the Kronecker product and $*$ stands for the linear convolution. Furthermore, $\mathbb{Z}^{x\times y}$, $\mathbb{R}^{x\times y}$, and $\mathbb{C}^{x\times y}$ denote the space of $x \times y$ integer-, real-, and complex-valued matrices, respectively; The $\log(\cdot)$ represents the logarithmic operation; while $\mathbb{E}(\cdot)$ stands for the expectation operation. The distribution of a circularly symmetric complex Gaussian (CSCG) random vector with mean vector $\boldsymbol{\mu}$ and covariance matrix $\boldsymbol{\Sigma}$ is denoted by $\mathcal{CN}(\boldsymbol{\mu}, \boldsymbol{\Sigma})$, while the distribution of a real-valued Gaussian random variable with mean μ and σ^2 is denoted by $\mathcal{N}(\mu, \sigma^2)$; $\sim$ stands for "distributed as". $\max\{a, b\}$ and $\min\{a, b\}$ denote the maximum and minimum between two real numbers a and b, respectively.

II. System Model

As illustrated in Fig. 2, we consider an OFDM wireless system, where multiple RISs are deployed on the facades

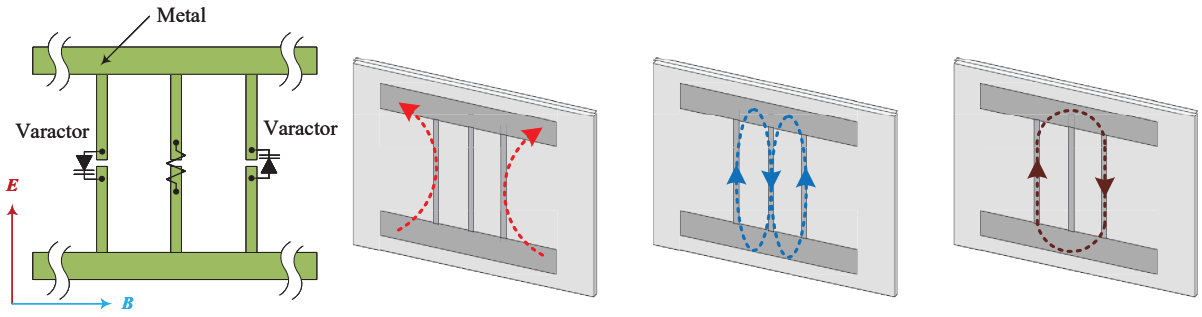

(a) Structure of a meta-atom. (b) Radiative mode. (c) Control mode. (d) Trapped mode.

Fig. 1. The adjustable-delay meta-atom and current flow for three operating modes.

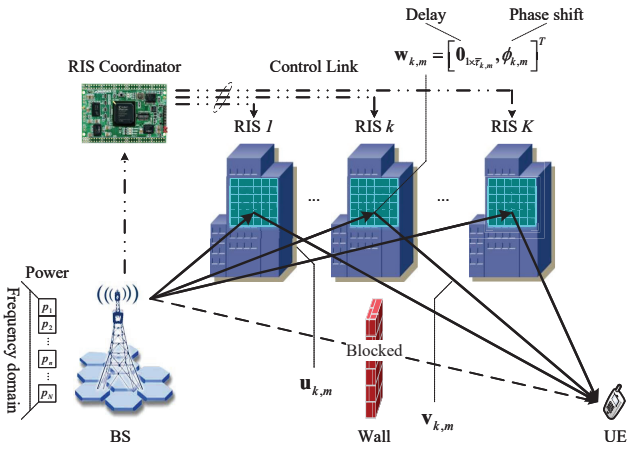

Fig. 2. The considered multiple-RIS assisted OFDM communication system.

of buildings or other environmental objects to assist in the end-to-end transmission between a BS and a cell-edge UE. We assume that the direct BS-UE path is blocked by a wall and that both the BS and the UE are equipped with a single antenna[2]. Explicitly, the total bandwidth allocated to the UE is equally divided into N orthogonal subcarriers, which are denoted by the set $\mathcal{N} = \{0, 1, \cdots, N-1\}$. Furthermore, the number of RISs is assumed to be K, indexed by the set $\mathcal{K} = \{1, 2, \cdots, K\}$. Each RIS comprises M passive reflecting elements, denoted by the set $\mathcal{M} = \{1, 2, \cdots, M\}$, and is connected to a smart RIS coordinator, which is capable of adjusting the RIS reflection patterns in real-time for desired signal propagation [12], [13]. In contrast to the existing reflecting elements, those considered in this paper can also impose an extra time delay on the incident signals to facilitate the coherent superposition of multiple copies of the desired signals and maintain their synchronization in time. Specifically, one of the feasible approaches is to cascade an existing phase-adjustable element [9] with an adjustable-delay element [54], as shown in Fig. 1(a). Moreover, we consider uplink channel training from the UE to the BS, where pilot symbols are sent from the UE and reflected by RISs. Based on these pilots, the BS estimates all cascaded BS-RIS-UE channels [27], [28]. For the downlink, we assume a time-division duplex (TDD) protocol for exploiting channel reciprocity. Then the reflection patterns can be readily optimized at the BS based on the CSI obtained during the uplink training and then inform all RISs via a separate wireless control link. Due to the severe path loss, it is further assumed that the power of the signals reflected by RISs more than once is negligible and thus ignored [10], [24].

We consider a quasi-static frequency-selective block fading channel model for all links involved in Fig. 2 and focus our attention on a particular fading block, where the channels remain approximately constant. Specifically, there exists an L_k-tap baseband equivalent multipath channel for the BS-RIS-UE link reflected via the k-th RIS. Then the signals transmitted by the BS are reflected by the k-th RIS before arriving at the UE. Specifically, let $\mathbf{u}_{k,m} \in \mathbb{C}^{L_{k,\mathrm{BR}} \times 1}$, $\forall m \in \mathcal{M}$, $\forall k \in \mathcal{K}$, denote the $L_{k,\mathrm{BR}}$-tap baseband equivalent channel spanning from the BS to the m-th reflecting element at the k-th RIS. Similarly, let $\mathbf{v}_{k,m} \in \mathbb{C}^{L_{k,\mathrm{RU}} \times 1}$, $\forall m \in \mathcal{M}$, $\forall k \in \mathcal{K}$, denote the $L_{k,\mathrm{RU}}$-tap baseband equivalent channel of the RIS-UE link associated with the m-th reflecting element at the k-th RIS. Thus, we have $L_k = L_{k,\mathrm{BR}} + L_{k,\mathrm{RU}} - 1$, $\forall k \in \mathcal{K}$. We assume that K RISs are sorted in an ascending order according to their distances from the direct link, which means that $L_1 \leq L_2 \leq \cdots \leq L_K$.

Furthermore, each RIS element is also capable of rescattering the impinging signals upon imposing an independent reflection coefficient and a tunable time delay, as previously stated. More specifically, let $\boldsymbol{\phi}_k = [\phi_{k,1}, \phi_{k,2}, \cdots, \phi_{k,M}]^T \in \mathbb{C}^{M \times 1}$, $\forall k \in \mathcal{K}$, denote the reflection coefficients at the k-th RIS, where each reflection coefficient $\phi_{k,m}$ characterizes the equivalent effect of the m-th element on the incident signals at the k-th RIS. More explicitly, each $\phi_{k,m}$ can be expressed as

$$\phi_{k,m} = \beta_{k,m} e^{j\theta_{k,m}}, \ \forall m \in \mathcal{M}, \ \forall k \in \mathcal{K}, \tag{1}$$

where $\beta_{k,m} \in [0, 1]$ denotes the amplitude coefficient while $\theta_{k,m} \in [0, 2\pi)$ stands for the phase shift of the m-th element at the k-th RIS, respectively. To maximize the reflected power of each RIS element and simplify its hardware design, we

[2]In this paper, the SISO scenario is considered for characterizing the maximum performance gain benefited from adjustable-delay RIS. When considering the scenarios that BS is equipped with multiple antennas, the adjustable RIS delays need to cater for all channels spanning from different antennas to the user. The design problem considering adjustable RIS delay under general MIMO setups is left as our future research topic.

fix $\beta_{k,m} = 1,\ \forall m \in \mathcal{M},\ \forall k \in \mathcal{K}$, and only adjust the phase shift $\theta_{k,m}$ for reflection pattern optimization in this paper, thus we have $\left|\phi_{k,m}\right| = 1$. Additionally, let $\boldsymbol{\tau}_k = \left[\tau_{k,1}, \tau_{k,2}, \cdots, \tau_{k,M}\right]^T \in \mathbb{R}^{M\times 1},\ \forall k \in \mathcal{K}$, denote the delay vector at the k-th RIS, where each $\tau_{k,m}$ characterizes the delay imposed by the m-th element at the k-th RIS. For practical adjustable-delay RIS operation, we have

$$0 \le \tau_{k,m} \le \tau_{\max},\ \forall m \in \mathcal{M},\ \forall k \in \mathcal{K}, \tag{2}$$

where $\tau_{\max}$ denotes the maximum time during which a RIS element can store and retrieve the impinging signals [54]. To elaborate, we assume that the tunable delay resolution at each reflecting element is equal to the sampling interval[3]. Specifically, let $\bar{\boldsymbol{\tau}}_k = \left[\bar{\tau}_{k,1}, \bar{\tau}_{k,2}, \cdots, \bar{\tau}_{k,M}\right]^T \in \mathbb{Z}^{M\times 1},\ \forall k \in \mathcal{K}$, denote the normalized delays at the k-RIS, where $\bar{\tau}_{k,m} = \left\lfloor \tau_{k,m} f_s \right\rceil,\ \forall m \in \mathcal{M},\ \forall k \in \mathcal{K}$, denotes the discrete delay incurred by the m-th element at the k-th RIS, while f_s represents the sampling rate. Thus, we have $0 \le \bar{\tau}_{k,m} \le \bar{\tau}_{\max},\ \forall m \in \mathcal{M},\ \forall k \in \mathcal{K}$, where $\bar{\tau}_{\max} = \lfloor \tau_{\max} f_s \rceil$ denotes the normalization of $\tau_{\max}$ with respect to f_s. As a result, the whole effect caused by the m-th reflecting element at the k-th RIS can be expressed by

$$\mathbf{w}_{k,m} = \left[\mathbf{0}_{1\times\bar{\tau}_{k,m}}, \phi_{k,m}\right]^T,\ \forall m \in \mathcal{M},\ \forall k \in \mathcal{K}, \tag{3}$$

which will degenerate into a conventional reflecting element if we have $\bar{\tau}_{k,m} = 0$. Moreover, note that here we do not take into account any power loss of the adjustable-delay RIS in the resource allocation design. However, the power attenuation caused by adjustable-delay RIS for practical implementation will be evaluated through our simulations in Section VI.

Hence, the channel impulse response (CIR) of the BS-RIS-UE link reflected by the m-th reflecting element at the k-th RIS is thus the concatenation of the BS-RIS channel, RIS's rotation and delay, as well as the RIS-UE channel, which is given by $\mathbf{u}_{k,m} * \mathbf{w}_{k,m} * \mathbf{v}_{k,m} = \mathbf{w}_{k,m} * \mathbf{u}_{k,m} * \mathbf{v}_{k,m} \in \mathbb{C}^{(\bar{\tau}_{k,m}+L_k)\times 1},\ \forall m \in \mathcal{M},\ \forall k \in \mathcal{K}$. For the sake of exposition, we define $\mathbf{H}_k = \left[\mathbf{h}_{k,1}, \mathbf{h}_{k,2}, \cdots, \mathbf{h}_{k,M}\right] \in \mathbb{C}^{N\times M},\ \forall k \in \mathcal{K}$, as the zero-padded concatenated BS-RIS-UE channels without any regard to the k-th RIS's effect, where we have $\mathbf{h}_{k,m} = \left[\left(\mathbf{u}_{k,m} * \mathbf{v}_{k,m}\right)^T, \mathbf{0}_{1\times(N-L_k)}\right]^T \in \mathbb{C}^{N\times 1},\ \forall m \in \mathcal{M},\ \forall k \in \mathcal{K}$. The composite BS-RIS-UE channel of all M links reflected by the k-th RIS, denoted by $\mathbf{g}_k \in \mathbb{C}^{N\times 1}$, can thus be expressed as

$$\mathbf{g}_k = \sum_{m=1}^{M} \phi_{k,m}\mathbf{S}_{k,m}\mathbf{h}_{k,m} = \mathbf{S}_k\boldsymbol{\Phi}_k\mathbf{h}_k,\ \forall k \in \mathcal{K}, \tag{4}$$

where we have

$$\mathbf{S}_{k,m} = \left[\mathbf{0}_{\bar{\tau}_{k,m}\times(N-\bar{\tau}_{k,m})}, \mathbf{I}_{\bar{\tau}_{k,m}}; \mathbf{I}_{N-\bar{\tau}_{k,m}}, \mathbf{0}_{(N-\bar{\tau}_{k,m})\times\bar{\tau}_{k,m}}\right],$$

$\mathbf{S}_k = \left[\mathbf{S}_{k,1}, \mathbf{S}_{k,2}, \cdots, \mathbf{S}_{k,M}\right]$, $\boldsymbol{\Phi}_k = \mathrm{diag}\left(\boldsymbol{\phi}_k\right) \otimes \mathbf{I}_N$, $\mathbf{h}_k = \mathrm{vec}\left(\mathbf{H}_k\right) = \left[\mathbf{h}_{k,1}^T, \mathbf{h}_{k,2}^T, \cdots, \mathbf{h}_{k,M}^T\right]^T$. We note that $\boldsymbol{\Phi}_k$ and $\mathbf{S}_k$ characterize the effect of reflection coefficients and delays of the k-th RIS, respectively. Therefore, the composite CIR spanning from the BS to the UE is the superposition of all reflected BS-RIS-UE channels, which is given by

$$\tilde{\mathbf{g}} = \sum_{k=1}^{K} \mathbf{g}_k = \sum_{k=1}^{K} \mathbf{S}_k\boldsymbol{\Phi}_k\mathbf{h}_k = \sum_{k=1}^{K}\sum_{m=1}^{M} \phi_{k,m}\mathbf{S}_{k,m}\mathbf{h}_{k,m}. \tag{5}$$

Next, let us consider the OFDM downlink. Specifically, let $\mathbf{p} = [p_0, p_1, \cdots, p_{N-1}]^T \in \mathbb{R}^{N\times 1}$, where $p_n \ge 0,\ \forall n \in \mathcal{N}$, denotes the power allocated to the n-th subcarrier at the BS. Assume furthermore that the aggregate transmit power available at the BS is P. Thus, the power allocation solution should satisfy $\sum_{n=0}^{N-1} p_n \le P$. Furthermore, let $\mathbf{x} = [x_0, x_1, \cdots, x_{N-1}]^T$ denote the normalized OFDM symbol, which is first transformed into the time domain via an N-point inverse discrete Fourier transform (IDFT), and then extended by a CP of length N_{CP}, which is assumed to be longer than the maximum delay spread of all reflected BS-RIS-UE channels, i.e., $N_{CP} \ge L_K$.

After removing the CP and performing the N-point discrete Fourier transform (DFT) at the UE receiver, the equivalent baseband signal received in the frequency domain is given by

$$\mathbf{y} = \mathbf{X}\mathbf{P}^{1/2}\mathbf{F}\tilde{\mathbf{g}} + \mathbf{z} = \mathbf{X}\mathbf{P}^{1/2}\mathbf{F}\sum_{k=1}^{K}\sum_{m=1}^{M} \phi_{k,m}\mathbf{S}_{k,m}\mathbf{h}_{k,m} + \mathbf{z}, \tag{6}$$

where $\mathbf{y} = [y_0, y_1, \cdots, y_{N-1}]^T \in \mathbb{C}^{N\times 1}$ is the OFDM symbol received in the frequency domain; $\mathbf{X} = \mathrm{diag}\left(\mathbf{x}\right)$ and $\mathbf{P} = \mathrm{diag}\left(\mathbf{p}\right)$ denote the diagonal matrix of the transmit OFDM symbol $\mathbf{x}$ and the power allocation solution $\mathbf{p}$, respectively; $\mathbf{z} = [z_0, z_1, \cdots, z_{N-1}]^T \sim \mathcal{CN}\left(\mathbf{0}, \sigma^2\mathbf{I}_N\right)$ is the additive white Gaussian noise (AWGN) vector in the frequency domain with σ^2 denoting the average noise power on each subcarrier; $\mathbf{F} \in \mathbb{C}^{N\times N}$ is the DFT matrix.

Specifically, the channel's frequency response (CFR) at the n-th subcarrier is given by

$$d_n = \mathbf{f}_n^H \sum_{k=1}^{K}\sum_{m=1}^{M} \phi_{k,m}\mathbf{S}_{k,m}\mathbf{h}_{k,m},\ \forall n \in \mathcal{N}, \tag{7}$$

where $\mathbf{f}_n^H$ denotes the n-th row of the DFT matrix $\mathbf{F}$. Therefore, the achievable rate of RIS-aided OFDM systems in terms of bits per second per Hertz (b/s/Hz) is given by

$$R\left(\mathbf{p}, \boldsymbol{\phi}, \bar{\boldsymbol{\tau}}\right) = \frac{\sum_{n=0}^{N-1} \log_2\left(1 + \frac{\left|\mathbf{f}_n^H \sum_{k=1}^{K}\sum_{m=1}^{M} \phi_{k,m}\mathbf{S}_{k,m}\mathbf{h}_{k,m}\right|^2 p_n}{\Gamma\sigma^2}\right)}{N + N_{CP}}, \tag{8}$$

where we have $\boldsymbol{\phi} = \left[\boldsymbol{\phi}_1^T, \boldsymbol{\phi}_2^T, \cdots, \boldsymbol{\phi}_K^T\right]^T \in \mathbb{C}^{MK\times 1}$ and $\bar{\boldsymbol{\tau}} = \left[\bar{\boldsymbol{\tau}}_1^T, \bar{\boldsymbol{\tau}}_2^T, \cdots, \bar{\boldsymbol{\tau}}_K^T\right]^T \in \mathbb{Z}^{MK\times 1}$, while $\Gamma \ge 1$ characterizes the gap from Shannon's capacity owing to using a discrete modulation and coding scheme.

Remark 1: Note that in contrast to the conventional RIS-assisted OFDM systems that use a common phase shift for each RIS element to cater for all subcarriers [27], [28], the new design DoF, $\mathbf{S}_{k,m}$, introduced in (8) is capable of adjusting the RIS delay thus imposing differentiated impacts on the channel responses of different subcarriers. Therefore, the adjustable-delay RIS enables the coherent superposition of different reflected links on all subcarriers. The specific $\mathbf{S}_{k,m}$ will be designed by our algorithms proposed in Sections IV and V.

[3]In fact, the adjustable delay resolution depends on the specific hardware design, which, anyhow, generally leads to grid mismatch errors in time synchronization [54]. Fortunately, with the employment of millimeter-wave and terahertz frequency bands, the mismatch errors will be substantially eliminated due to the higher sampling rate.

Remark 2: To maximize the achievable rate of the RIS-aided OFDM systems considered, accurate knowledge of the CSI, i.e., $\{\mathbf{H}_1, \mathbf{H}_2, \cdots, \mathbf{H}_K\}$, is required at the cost of extra channel training and feedback overhead. Fortunately, the achievable rate relies only on the CSI of the cascaded reflection channels, and several sophisticated channel estimation approaches have been proposed in [27], [34], [59] for RIS-aided OFDM systems by employing the grouping-based philosophy, channel sparsity, etc. To elaborate, in the following, we assume that the CSI of all reflected channels is known *a priori* while the effects of channel estimation errors will be detailed based on our simulations in Section VI.

III. Achievable Rate Maximization Problem Formulation

Given all reflected BS-RIS-UE channel matrices, i.e., $\{\mathbf{H}_1, \mathbf{H}_2, \cdots, \mathbf{H}_K\}$, we aim for maximizing the achievable rate shown in (8) by jointly optimizing the transmit power allocation $\mathbf{p}$, the RIS reflection coefficients $\boldsymbol{\phi}$, as well as the RIS delays $\bar{\boldsymbol{\tau}}$. Therefore, we formulate the following optimization problem, where the constant terms in (8) are omitted for brevity, yielding

$$(P1): \max_{\mathbf{p},\boldsymbol{\phi},\bar{\boldsymbol{\tau}}} \sum_{n=0}^{N-1} \log_2\left(1+\frac{\left|\mathbf{f}_n^H \sum_{k=1}^{K}\sum_{m=1}^{M} \phi_{k,m}\mathbf{S}_{k,m}\mathbf{h}_{k,m}\right|^2 p_n}{\Gamma\sigma^2}\right) \tag{9a}$$

$$\text{s.t.} \sum_{n=0}^{N-1} p_n \le P, \tag{9b}$$

$$p_n \ge 0,\ \forall n \in \mathcal{N}, \tag{9c}$$

$$\left|\phi_{k,m}\right| = 1,\ \forall m \in \mathcal{M},\ \forall k \in \mathcal{K}, \tag{9d}$$

$$0 \le \bar{\tau}_{k,m} \le \bar{\tau}_{\max},\ \forall m \in \mathcal{M},\ \forall k \in \mathcal{K}, \tag{9e}$$

$$L_k + \bar{\tau}_{k,m} \le N_{CP},\ \forall m \in \mathcal{M},\ \forall k \in \mathcal{K}, \tag{9f}$$

where (9b) and (9c) characterize the limitations on transmit power allocation; (9d) denotes the constant-modulus RIS phase shift; (9e) and (9f) guarantee that the maximum delay spread after introducing extra RIS delays will not exceed the length of the CP. We note that Problem $(P1)$ is a non-convex optimization problem. Explicitly, it can be shown that the objective function (9a) is non-concave over $\boldsymbol{\phi}$ and $\bar{\boldsymbol{\tau}}$; Moreover, the variables $\mathbf{p}$, $\boldsymbol{\phi}$, and $\bar{\boldsymbol{\tau}}$ are coupled in the objective function (9a), which makes their joint optimization difficult. To overcome the above challenges, next, we will propose an AO algorithm to find a high-quality near-optimal solution for Problem $(P1)$, by iteratively optimizing either $\mathbf{p}$ or $\{\boldsymbol{\phi}, \bar{\boldsymbol{\tau}}\}$ with the other one fixed at each time.

IV. Joint Transmit Power Allocation and Reflection Pattern Optimization

A. Transmit Power Allocation Given the RIS Reflection Pattern

Note that given a set of RIS reflection patterns $\{\boldsymbol{\phi}, \bar{\boldsymbol{\tau}}\}$ as well as the CSI, the optimization problem in (9) can be reduced to

$$(P2): \max_{\mathbf{p}} \sum_{n=0}^{N-1} \log_2\left(1+\frac{\left|\mathbf{f}_n^H \sum_{k=1}^{K}\sum_{m=1}^{M} \phi_{k,m}\mathbf{S}_{k,m}\mathbf{h}_{k,m}\right|^2 p_n}{\Gamma\sigma^2}\right) \tag{10a}$$

$$\text{s.t. (13a), (13b).} \tag{10b}$$

The optimal transmit power allocation $\mathbf{p}^o$ at the BS is thus given by the well-known water-filling solution, which assigns more power to the high-quality channels [19], i.e.,

$$p_n^o = \left(c - \frac{\Gamma\sigma^2}{|d_n|^2}\right)^+,\ \forall n \in \mathcal{N}, \tag{11}$$

where we have $(a)^+ \triangleq \max(0, a)$, while c is the cut-off power threshold, so that $\sum_{n=0}^{N-1} p_n^o = P$, which can be found by employing the popular bisection search.

B. RIS Reflection Pattern Optimization Given the Transmit Power Allocation

Given a tentative transmit power allocation solution, Problem $(P1)$ is thus simplified to

$$(P3): \max_{\boldsymbol{\phi},\bar{\boldsymbol{\tau}}} \sum_{n=0}^{N-1} \log_2\left(1+\frac{\left|\mathbf{f}_n^H \sum_{k=1}^{K}\sum_{m=1}^{M} \phi_{k,m}\mathbf{S}_{k,m}\mathbf{h}_{k,m}\right|^2 p_n}{\Gamma\sigma^2}\right) \tag{12a}$$

$$\text{s.t. (13d), (13e), (13f).} \tag{12b}$$

It can be shown that Problem $(P3)$ is still a non-convex one and thus non-trivial to be maximized. Alternatively, we consider maximizing a tight upper bound of (12a) instead. Specifically, the achievable rate shown in (8) is upper-bounded by

$$R(\mathbf{p}, \boldsymbol{\phi}, \bar{\boldsymbol{\tau}}) \le \frac{N\log_2\left(1+\frac{\sum_{n=0}^{N-1}\left|\mathbf{f}_n^H \sum_{k=1}^{K}\sum_{m=1}^{M} \phi_{k,m}\mathbf{S}_{k,m}\mathbf{h}_{k,m}\right|^2 p_n}{N\Gamma\sigma^2}\right)}{N+N_{CP}}, \tag{13}$$

based on Jensen's inequality. In fact, the upper bound of $R(\mathbf{p}, \boldsymbol{\phi}, \bar{\boldsymbol{\tau}})$ on the right-hand-side (RHS) of (13) is tight at high signal-to-noise-ratios (SNR), which is indeed the case under massive RIS deployment. Explicitly, Fig. 3(a) compares the achievable rate of (8) and its upper bound of (13), where we consider only a single RIS and the equal power allocation for the sake of illustration. Observe from Fig. 3(a) that the RHS of (13) is an extremely tight upper bound of the achievable rate of (8), especially for a RIS having a large number of reflecting elements. Therefore, the maximization of the RHS of (13) is almost equivalent to the original Problem $(P3)$.

After removing the constant terms, the new optimization problem is formulated as follows:

$$(P3\text{-UB}): \max_{\boldsymbol{\phi},\bar{\boldsymbol{\tau}}} \sum_{n=0}^{N-1}\left|\mathbf{f}_n^H \sum_{k=1}^{K}\sum_{m=1}^{M} \phi_{k,m}\mathbf{S}_{k,m}\mathbf{h}_{k,m}\right|^2 p_n \tag{14a}$$

$$\text{s.t. (13d), (13e), (13f),} \tag{14b}$$

which turns out to be the maximization of the weighted sum of CFRs at the receiver.

Furthermore, note that for a given tentative delay vector $\bar{\boldsymbol{\tau}}$, Problem $(P3\text{-UB})$ reduces to

$$(P4): \max_{\boldsymbol{\phi}} \sum_{n=0}^{N-1}\left|\mathbf{f}_n^H \sum_{k=1}^{K}\sum_{m=1}^{M} \phi_{k,m}\mathbf{S}_{k,m}\mathbf{h}_{k,m}\right|^2 p_n \tag{15a}$$

$$\text{s.t. (13d),} \tag{15b}$$

Algorithm 1: Alternating Optimization (AO) Algorithm for Solving Problem $(P1)$

1: **Input:** $\{\mathbf{H}_1, \mathbf{H}_2, \cdots, \mathbf{H}_K\}$, Γ, σ^2.
2: Randomly generate multiple initializations, i.e., $\left\{\mathbf{p}^{(1)}, \mathbf{p}^{(2)}, \cdots, \mathbf{p}^{(J)}\right\}$;
3: **for** $\mathbf{p}^{(j)},\ 1 \le j \le J$, **do**
4: **for** $\bar{\boldsymbol{\tau}} \in \mathcal{A}$, **do**
5: Solve Problem $(P4\text{-SDR})$ based on the given $\mathbf{p}$ and $\bar{\boldsymbol{\tau}}$ via CVX;
6: Apply Gaussian randomization to find an approximate $\boldsymbol{\phi}$ of Problem $(P4\text{-E})$;
7: **end for**
8: Solve Problem $(P5)$ to select the optimal $\bar{\boldsymbol{\tau}}$ and $\boldsymbol{\phi}$;
9: Solve Problem $(P2)$ to obtain the optimal $\mathbf{p}$ based on $\{\boldsymbol{\phi}, \bar{\boldsymbol{\tau}}\}$;
10: **while** The objective value of (9a) with the obtained $\mathbf{p}^o$, $\boldsymbol{\phi}^o$ and $\bar{\boldsymbol{\tau}}^o$ reaches convergence;
11: **Output:** The optimal $\{\mathbf{p}^o, \boldsymbol{\phi}^o, \bar{\boldsymbol{\tau}}^o\}$ maximizing the achievable rate of (8) from J candidates.

which can be further simplified to

$$(P4\text{-E}):\ \max_{\boldsymbol{\phi}}\ \left\|\mathbf{P}^{1/2}\mathbf{F}\mathbf{T}\boldsymbol{\phi}\right\|^2 \tag{16a}$$

$$\text{s.t. (13d)}, \tag{16b}$$

where $\mathbf{T}$ is defined by $\mathbf{T} = \left[\mathbf{S}_{1,1}\mathbf{h}_{1,1}, \cdots, \mathbf{S}_{1,M}\mathbf{h}_{1,M}, \cdots, \mathbf{S}_{K,1}\mathbf{h}_{K,1}, \cdots, \mathbf{S}_{K,M}\mathbf{h}_{K,M}\right]$. Note that Problem $(P4\text{-E})$ is a non-convex quadratically constrained quadratic problem (QCQP), for which we can apply the classic semidefinite relaxation (SDR) [10], [27] technique to obtain an approximate solution. Specifically, upon defining $\boldsymbol{\Psi} = \boldsymbol{\phi}\boldsymbol{\phi}^H$ and $\mathbf{R} = \mathbf{T}^H\mathbf{F}^H\mathbf{P}\mathbf{F}\mathbf{T}$, we transform Problem $(P4\text{-E})$ into the following problem by relaxing the rank-one constraint, i.e.,

$$(P4\text{-SDR}):\ \max_{\boldsymbol{\phi}}\ \mathrm{tr}\left(\mathbf{R}\boldsymbol{\Psi}\right) \tag{17a}$$

$$\text{s.t. } \boldsymbol{\Psi}_{i,i} = 1,\ 1 \le i \le MK, \tag{17b}$$

$$\boldsymbol{\Psi} \succeq \mathbf{0}. \tag{17c}$$

Problem $(P4\text{-SDR})$ is a convex semidefinite programming (SDP) problem, which can be efficiently solved via existing convex optimization software, e.g., CVX [60]. Let $\boldsymbol{\Psi}^o$ denote the optimal solution of Problem $(P4\text{-SDR})$. If we have $\mathrm{rank}\left(\boldsymbol{\Psi}^o\right) = 1$, the relaxation from Problem $(P4\text{-E})$ to Problem $(P4\text{-SDR})$ is tight and the optimal $\boldsymbol{\phi}$ to Problem $(P4\text{-E})$ can be obtained by $\boldsymbol{\phi} = \mathbf{U}\mathrm{diag}\left(\boldsymbol{\Lambda}^{1/2}\right)$, where $\boldsymbol{\Psi}^o = \mathbf{U}\boldsymbol{\Lambda}\mathbf{U}^H$ is the eigenvalue decomposition (EVD) of the matrix $\boldsymbol{\Psi}^o$. By contrast, if $\mathrm{rank}\left(\boldsymbol{\Psi}^o\right) > 1$ holds, the optimal objective value of Problem $(P4\text{-SDR})$ serves as an upper bound to that of Problem $(P4\text{-E})$ and thus we have to construct a rank-one solution according to $\boldsymbol{\Psi}^o$. In this paper, we consider a customized Gaussian randomization method [10] to find an approximate solution to Problem $(P4\text{-E})$. Specifically, a number (denoted by Q) of $\boldsymbol{\phi}$ are generated by $\boldsymbol{\phi}_q = \mathbf{U}\mathrm{diag}\left(\boldsymbol{\Lambda}^{1/2}\right)\boldsymbol{\delta},\ q = 1, 2, \cdots, Q$, where $\boldsymbol{\delta} \sim \mathcal{CN}\left(\mathbf{0}, \mathbf{I}_{KM}\right)$ is a complex-valued Gaussian random vector. Following this, a sub-optimal reflection coefficient solution to Problem $(P4\text{-E})$ is thus obtained by selecting the one from $\left\{\boldsymbol{\phi}_1, \boldsymbol{\phi}_2, \cdots, \boldsymbol{\phi}_Q\right\}$ that maximizes the objective value of (16a).

For each legitimate $\bar{\boldsymbol{\tau}}$, we repeatedly solve the Problem $(P4\text{-E})$ formulated. After finding a sub-optimal $\boldsymbol{\phi}$ for all feasible $\bar{\boldsymbol{\tau}}$, the optimal solution of $\bar{\boldsymbol{\tau}}$ can be readily obtained by solving

$$(P5):\ \max_{\bar{\boldsymbol{\tau}}}\ \left\|\mathbf{P}^{1/2}\mathbf{F}\mathbf{T}\left(\bar{\boldsymbol{\tau}}\right)\boldsymbol{\phi}\left(\bar{\boldsymbol{\tau}}\right)\right\|^2 \tag{18a}$$

$$\text{s.t. } 0 \le \bar{\tau}_{k,m} \le \bar{\tau}'_k,\ \forall m \in \mathcal{M},\ \forall k \in \mathcal{K}, \tag{18b}$$

where we have $\bar{\tau}'_k = \min\left(\bar{\tau}_{\max}, N_{CP} - L_k\right)$. We note that Problem $(P5)$ can be readily solved by searching over all legitimate delay vectors. Since there is not much delay difference amongst the different channels reflected via the same RIS of moderate size, we can reduce the complexity of solving Problem $(P5)$ by searching for a common delay for each RIS. The relationship between the tolerable delay and its corresponding RIS size is detailed in Section V-B. For each RIS, the scope of the adjustable delay does not exceed the CP margin. Let $\bar{\boldsymbol{\tau}}^o$ denote the optimal solution of Problem $(P5)$. Thus the high-quality sub-optimal solution of Problem $(P3\text{-UB})$ is given by $\{\bar{\boldsymbol{\tau}}^o, \boldsymbol{\phi}\left(\bar{\boldsymbol{\tau}}^o\right)\}$.

In summary, the overall AO procedure of solving Problem $(P1)$ is given in Algorithm 1, where $\mathcal{A}$ in line 4 is defined by $\mathcal{A} = \left[0, \bar{\tau}'_1\right]^M \times \left[0, \bar{\tau}'_2\right]^M \times \cdots \times \left[0, \bar{\tau}'_K\right]^M$. We note that the AO algorithm might fall into a locally optimal solution. Hence, in Algorithm 1, we provide a heuristic method to address this problem upon adopting multiple (denoted by J) random initializations [24], which guarantees that Algorithm 1 finds at least a high-quality sub-optimal solution of the original Problem $(P1)$. Note that the complexity of Algorithm 1 is critically high. In the next section, we will propose a low-complexity method for efficiently solving Problem $(P1)$.

V. A Low-Complexity Optimization Method for Power Allocation and Reflection Coefficient Optimization

A. The Proposed Low-Complexity Method

Although the AO algorithm achieves near-optimal performance, its complexity of solving Problem $(P1)$ is shown in [10], [28] to be on the order of $\mathcal{O}\left(JN_iK^{4.5}M^{4.5}\prod_{k=1}^{K}\bar{\tau}'_k\right)$, where J represents the number of random initializations. Furthermore, N_i represents the number of iterations, $\mathcal{O}\left(K^{4.5}M^{4.5}\right)$ characterizes the complexity order of solving Problem $(P4\text{-SDR})$ at each iteration, while $\bar{\tau}'_k$ is the cardinality of the feasible delay set associated with the k-th RIS. We note that the complexity of Algorithm 1 becomes excessive for large values of K and M. Hence, in this subsection, we propose a low-complexity method to solve Problem $(P1)$ suboptimally by focusing on the delay domain. Specifically, for a typical wireless channel, we have $L_K \le N_{CP} \ll N$, which implies that the channel gain is much more concentrated to a limited interval in the delay domain than in the frequency domain. Therefore, upon exploiting Parseval's theorem and omitting the transmit power allocation, the objective function of (14a) can be transformed into the delay domain, yielding

$$(P6):\ \max_{\boldsymbol{\phi},\bar{\boldsymbol{\tau}}}\ \sum_{n=0}^{N-1}\left|\sum_{k=1}^{K}\sum_{m=1}^{M}\phi_{k,m}\mathbf{S}_{k,m}\mathbf{h}_{k,m}\right|^2 \tag{19a}$$

$$\text{s.t. (13d)},\ \text{(13e)},\ \text{(13f)}. \tag{19b}$$

Next, we propose our low-complexity method by adjusting the RISs' reflection coefficients and delays to align the strongest CIR tap of all reflected channels, while ensuring that

Algorithm 2: The Low-Complexity Strongest Tap Alignment (STA) Method for Solving Problem $(P1)$

1: **Input:** $\{\mathbf{H}_1, \mathbf{H}_2, \cdots, \mathbf{H}_K\}$, Γ, σ^2.
2: Find the strongest tap for each reflected channel by (20);
3: Update the strongest tap into a feasible scope by (21);
4: Calculate the RISs' coefficients $\boldsymbol{\phi}^o$ and delays $\bar{\boldsymbol{\tau}}^o$ by (22);
5: Perform the water-filling algorithm to obtain $\mathbf{p}^o$;
6: **Output:** $\{\mathbf{p}^o, \boldsymbol{\phi}^o, \bar{\boldsymbol{\tau}}^o\}$.

the maximum delay spread after adding extra delay does not exceed the length of the CP. Specifically, we first find the CIR tap, denoted by $\hat{l}_{k,m},\ \forall m \in \mathcal{M},\ \forall k \in \mathcal{K}$, having the highest CIR gain with respect to the m-th element at the k-th RIS, i.e.,

$$\hat{l}_{k,m} = \arg \max_{l_{k,m} \in \{1,2,\cdots,L_k\}} \left|\mathbf{h}_{k,m}\left(l_{k,m}\right)\right|^2. \tag{20}$$

Furthermore, in order to eliminate the inter-symbol interference, we have to ensure that the maximum difference of indices found by (20) is within the range of the adjustable delay. To achieve this, we search again for the strongest tap within a feasible CIR-support range determined by the maximum index value of $\hat{l}_{\max} = \max_{m \in \mathcal{M}, k \in \mathcal{K}} \left\{\hat{l}_{k,m}\right\}$, i.e.,

$$\tilde{l}_{k,m} = \arg \max_{l_{k,m} \in \mathcal{L}_k} \left|\mathbf{h}_{k,m}\left(l_{k,m}\right)\right|^2,\ \forall m \in \mathcal{M},\ \forall k \in \mathcal{K}, \tag{21}$$

where we have $\mathcal{L}_k = \left\{\hat{l}_{\max} - \bar{\tau}'_k, \hat{l}_{\max} - \bar{\tau}'_k + 1, \cdots, \hat{l}_{\max}\right\}$. Hence, the suboptimal reflection coefficients $\phi^o_{k,m}$ and delays $\bar{\tau}^o_{k,m}$, $\forall m \in \mathcal{M},\ \forall k \in \mathcal{K}$ found for aligning the strongest taps are given by

$$\phi^o_{k,m} = e^{-j\angle \mathbf{h}_{k,m}(\tilde{l}_{k,m})},\ \bar{\tau}^o_{k,m} = \tilde{l}_{\max} - \tilde{l}_{k,m}, \tag{22}$$

respectively, where we have $\tilde{l}_{\max} = \max_{m \in \mathcal{M}, k \in \mathcal{K}} \left\{\tilde{l}_{k,m}\right\}$.

After obtaining the RISs' reflection coefficients and delays, the optimal water-filling solution is invoked to carry out the transmit power allocation, as described in Section IV-A. The detailed procedure of this low-complexity method is summarized in Algorithm 2, which is referred to as the strongest tap alignment (STA) method. The complexity of the STA method is on the order of $O\left(M \sum_{k=1}^{K} L_k\right)$, which is significantly reduced compared to that of Algorithm 1. It is worth pointing out that [28] introduced the method of aligning the taps of all reflected channels resulting in the largest sum of the CIR gains in the absence of adjustable-delay RIS, namely, adjusting only the RIS reflection coefficients via (22) upon substituting the index value of $\tilde{l} = \arg \max_{l \in \{0,1,\cdots,L_K\}} \left|\sum_{k=1}^{K} \sum_{m=1}^{M} \left|\mathbf{h}_{k,m}\left(l\right)\right|\right|^2$ for $\forall m \in \mathcal{M},\ \forall k \in \mathcal{K}$, which constitutes a lower bound of our STA method due to the fact that the sum of the maximum is higher than the maximum of the sum. The improved performance gain is a benefit of the extra design DoF constituted by the delay.

B. Theoretical Analysis

Next, we will theoretically verify the benefits of adjustable-delay RIS. Specifically, the effects of adjustable-delay RIS upon considering all reflected channels having only a non-zero tap are summarized in ***Lemma 1***, where only a single reflecting element is assumed at each RIS for the sake of illustration.

Lemma 1: Let $\mathbf{h}_k = |h_k|\, e^{j\angle h_k} \mathbf{e}_{L_k} \in \mathbb{C}^{N \times 1},\ k \in \mathcal{K}$, denote the CIR of the k-th reflected BS-RIS-UE channel. Hence, adjustable-delay RIS is capable of ensuring the perfectly coherent superposition of K reflected copies on all subcarriers. Explicitly, the optimal reflection coefficient and delay for the k-th RIS element are given by $\phi_k = e^{-j\angle h_k},\ \bar{\tau}_k = L_K - L_k,\ k \in \mathcal{K}$, respectively.

Proof: We assume $L_1 \leq L_2 \leq \cdots \leq L_K$. Then the CFR of the k-th reflected channel at the n-th subcarrier is given by

$$d_{n,k} = \mathbf{f}_n^H \mathbf{h}_k = \mathbf{f}_n^H\, |h_k|\, e^{j\angle h_k} \mathbf{e}_{L_k},\ \forall k \in \mathcal{K},\ \forall n \in \mathcal{N}. \tag{23}$$

In order to facilitate the coherent superposition of the CFR of the k-th channel and the K-th channel on the n-th subcarrier, the reflection coefficient $\kappa_{n,k},\ \forall k \in \mathcal{K},\ \forall n \in \mathcal{N}$ at the k-th RIS catering for the n-th subcarrier can be expressed as

$$\kappa_{n,k} = \frac{d_{n,K}/d_{n,k}}{|d_{n,K}/d_{n,k}|} = e^{j\angle h_K} e^{-j\angle h_k} \mathbf{f}_n^H \mathbf{e}_{L_K} \mathbf{e}_{L_k}^H \mathbf{f}_n. \tag{24}$$

It can be readily seen that if and only if $\mathbf{e}_{L_1} = \mathbf{e}_{L_2} = \cdots = \mathbf{e}_{L_K}$, $\kappa_{n,k}$ is independent of n, then we have $\phi_k = e^{-j\angle h_k},\ \bar{\tau}_k = L_K - L_k,\ k \in \mathcal{K}$. Since we have $L_K \leq N_{CP}$, the lengths of all CIRs after adding extra delays will not exceed the length of the CP. The proof is completed. ■

Lemma 1 demonstrates that for single-tap reflected channels, adjustable-delay RIS is capable of facilitating perfectly coherent superposition of all reflected channels on all subcarriers. Although the single-tap assumption in ***Lemma 1*** may seem restrictive, in practical systems, the BS-RIS and RIS-UE channels are generally of line-of-sight (LoS) nature, with a large proportion of power in the LoS path [10], [12]. In this sense, the role of adjustable-delay RIS is to align these LoS components of different reflected channels, especially for the distributed RIS deployment resulting in distinctly different delays.

Furthermore, even if only a single RIS is adopted, the delays via different RIS elements are no longer negligible if the RIS's size is large. Specifically, upon considering a square RIS array employing M elements having an element spacing of d, the RIS size incurring negligible delay should satisfy $2\sqrt{2}\left(\sqrt{M} - 1\right) d < c/2f_s$, where $c = 3.0 \times 10^8$ m/s is the velocity of light. Therefore, we have $M < \left(c \Big/ 4\sqrt{2} f_s d + 1\right)^2 \approx c^2 \big/ 32 f_s^2 d^2$ characterizing the largest RIS size still resulting in negligible delay effects. Given an example considering the carrier frequency of $f_c = 3$ GHz and the sampling rate of $f_s = 50$ MHz, the maximum number of RIS elements having a tolerable time delay is $M_{\max} = 450$ for the RIS having half-wavelength spaced elements.

For the sake of illustration, Fig. 3(b) compares the composite CFR in the presence and absence of adjustable-delay RIS, where we consider three RISs, each equipped with a single reflecting element. Specifically, the channels reflected via the three RISs are characterized by $|h_1| = 1$, $\angle h_1 = 0$, $L_1 = 1$; $|h_2| = \frac{1}{2}$, $\angle h_2 = \frac{3}{4}\pi$, $L_2 = 2$; $|h_3| = \frac{1}{4}$, $\angle h_3 = \frac{3}{2}\pi$, $L_3 = 4$. The number of OFDM subcarriers is set to $N = 256$. It can be seen from Fig. 3(b) that adjustable-delay RIS is capable of facilitating the coherent superposition of CFRs of three reflected channels, thus providing a higher achievable rate. More specifically, the ergodic achievable rate of the

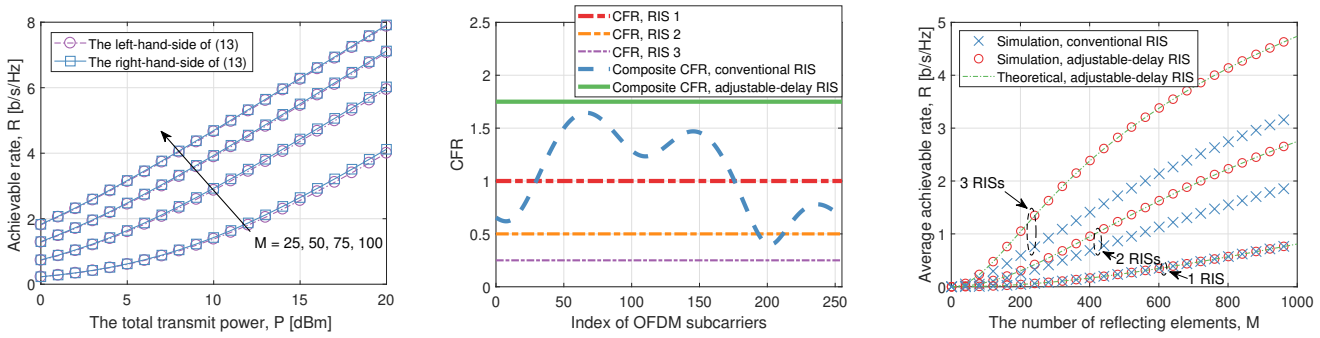

(a) (b) (c)

Fig. 3. (a) The comparison of the achievable rate of (8) and its tight upper bound of (13), where we have $K = 1$, $N = 1024$, $N_{CP} = 16$, $\sigma^2 = -100$ dBm, $\Gamma = 1$, $\rho^2 = -100$ dB, $L = 3$. (b) The CFRs of three reflected channels and their composite channel, where adjustable-delay RIS enables the coherent superposition of three channels on all subcarriers. (c) The rate comparison of RIS-aided OFDM systems in the presence/absence of adjustable-delay RIS, where we have $N = 1024$, $N_{CP} = 16$, $P = 15$ dBm, $\sigma^2 = -80$ dBm, $\Gamma = 1$, $\rho_1^2 = -115$ dB, $L_1 = 1$, $\rho_2^2 = -120$ dB, $L_2 = 2$, $\rho_3^2 = -125$ dB, $L_3 = 4$.

adjustable-delay RIS-aided OFDM systems is summarized in ***Lemma 2***.

Lemma 2: Let us assume that all single-tap reflected channels satisfy $h_{k,m} \sim \mathcal{CN}\left(0, \rho_k^2\right)$, $\forall m \in \mathcal{M}$, $\forall k \in \mathcal{K}$. As $M \to \infty$, the ergodic achievable rate of the adjustable-delay RIS-aided OFDM systems is given by

$$\mathbb{E}\left(R\right) = \frac{N}{N+N_{CP}} \log_2\left(1 + \frac{\left(\pi M^2 \left(\sum\limits_{k=1}^{K} \rho_k\right)^2 + (4-\pi) M \sum\limits_{k=1}^{K} \rho_k^2\right) P}{4N\Gamma\sigma^2}\right). \tag{25}$$

Proof: It can be readily shown that the composite channel retains the single-tap property, when relying on the reflection coefficients and delays given in ***Lemma 1***. Thus the composite CFR at each subcarrier can be formulated as:

$$d_0 = d_1 = \cdots = d_{N-1} = d = \sum_{k=1}^{K} \sum_{m=1}^{M} \left|h_{k,m}\right|. \tag{26}$$

Hence, the water-filling algorithm reduces to the equal power allocation, i.e., $p_0 = \cdots = p_{N-1} = P/N$.

Moreover, as $M \to \infty$, we have

$$d \sim \mathcal{N}\left(\frac{\sqrt{\pi}}{2} M \sum_{k=1}^{K} \rho_k, \frac{4-\pi}{4} M \sum_{k=1}^{K} \rho_k^2\right), \tag{27}$$

according to the central limit theorem [61]. Therefore, the ergodic achievable rate of the adjustable-delay RIS-aided OFDM systems is given by

$$\begin{aligned}\mathbb{E}\left(R\right) &= \mathbb{E}\left(\frac{N}{N+N_{CP}} \log_2\left(1 + \frac{d^2 P}{N\Gamma\sigma^2}\right)\right) \\ &\overset{M\to\infty}{\longrightarrow} \frac{N}{N+N_{CP}} \log_2\left(1 + \frac{\mathbb{E}\left(d^2\right) P}{N\Gamma\sigma^2}\right) \\ &= \frac{N}{N+N_{CP}} \log_2\left(1 + \frac{\left(\pi M^2 \left(\sum\limits_{k=1}^{K} \rho_k\right)^2 + (4-\pi) M \sum\limits_{k=1}^{K} \rho_k^2\right) P}{4N\Gamma\sigma^2}\right).\end{aligned} \tag{28}$$

The proof is completed. ■

Lemma 2 demonstrates that the adjustable-delay RIS-aided OFDM systems obey the quadratic power scaling law with M as for narrowband signals [10], [19]. For the sake of clarity, Fig. 3(c) verifies the accuracy of ***Lemma 2*** and compares the ergodic achievable rate of RIS-assisted OFDM systems both in the presence and absence of adjustable-delay RIS, where the specific simulation parameters are listed in Fig. 3(c). It can be observed that the ergodic achievable rate of adjustable-delay RIS-aided OFDM is higher than that of the conventional one relying on the traditional RIS by nearly 50%, when considering three RISs. Additionally, the theoretical analysis of ***Lemma 2*** perfectly matches the ergodic achievable rate of adjustable-delay RIS-assisted OFDM systems, even for the scenarios where the RISs involved have a small number of reflecting elements. Finally, we note that the proposed scheme employing a single RIS reduces to the conventional one [28].

VI. Simulation Results

A. Simulation Setup

In this section, we evaluate the performance of our proposed design and algorithms via numerical simulations. As shown in Fig. 4, we consider the OFDM downlink assisted by three RISs, all of which are assumed to have a uniform rectangular array consisting of M reflecting elements with half-wavelength spacing. The direct BS-UE link is assumed to be blocked. For ease of exposition, we assume that all RISs are placed along the x-z plane and perpendicular to the ground, i.e., to the x-y plane. The reference element's location of the k-th RIS is set to $\left(d_{\mathrm{BR}-x}, -k d_{\mathrm{BR}-y}, d_{\mathrm{R}-z}\right)$, $\forall k \in \mathcal{K}$, while the antennas' locations at the BS and the UE are set to $(0, 0, d_{\mathrm{B}-z})$ and $(d_{\mathrm{BU}-x}, 0, 0)$, respectively. In our simulations, the horizontal distance between the BS and all RISs is set to $d_{\mathrm{BR}-x} = 100$ m. The distance between different RISs is set to $d_{\mathrm{BR}-y} = 20$ m, while the height of the BS and all RISs is set to $d_{\mathrm{B}-z} = d_{\mathrm{R}-z} = 10$ m. Note that the locations of the practical RIS deployment are generally chosen to favor LoS propagation between the RISs and the BS/UE. Hence, for each RIS, the separate BS-RIS and RIS-UE links are both modeled by multi-path Rician fading channels with the first non-zero tap of each channel being the deterministic LoS path and the remaining

TABLE II
THE OPERATION SETUP OF 8 BENCHMARK SCHEMES.

Scheme	Power allocation	Delay	Phase shift	Abbr.	Ref.	Scheme	Power allocation	Delay	Phase shift	Abbr.	Ref.
1	Equal	NO	Statistical	Eq. & con. RIS & S		5	water-filling	NO	Statistical	WF & con. RIS & S	[20]
2	Equal	NO	Optimal	SDR, SCM	[28]	6	water-filling	NO	Optimal	WF & con. RIS & O	[27]
3	Equal	YES	Statistical	Eq. & AD-RIS & S		7	water-filling	YES	Statistical	WF & AD-RIS & S	
4	Equal	YES	Optimal	Eq. & AD-RIS & O		8	water-filling	YES	Optimal	Algorithm 2	

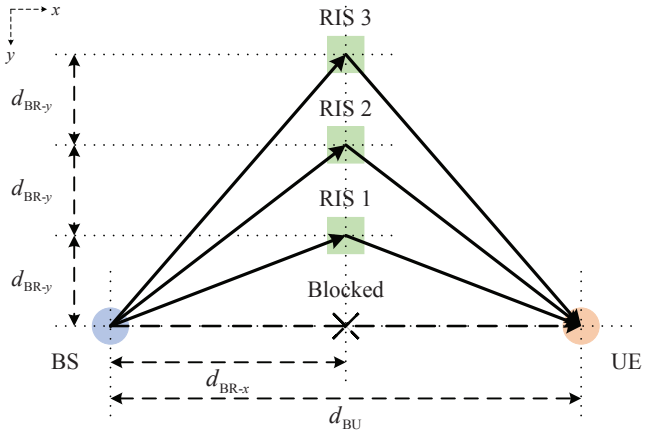

Fig. 4. The position setting of the BS, UE, and RISs (from the top view).

non-zero taps characterizing the non-LoS (NLoS) paths [36]. Explicitly, the maximum delay spread of the k-th BS-RIS link is set to $L_{k,\text{BR}} = L_{k,\text{BR}}^{\text{zero}} + L_{k,\text{BR}}^{\text{non-zero}}$, $\forall k \in \mathcal{K}$ taps, where the first $L_{k,\text{BR}}^{\text{zero}} = \lfloor d_{k,\text{BR}} f_s / c \rceil$ taps characterize the transmission delay of the BS-RIS link associated with the k-th RIS, while the last $L_{k,\text{BR}}^{\text{non-zero}}$ taps depend on the specific dispersive environment of the k-th BS-RIS channel. For the sake of illustration, we set $L_{k,\text{BR}}^{\text{non-zero}} = 1$ with a Rician factor of $\zeta_{k,\text{BR}} = \infty$, $\forall k \in \mathcal{K}$ (e.g., a macro BS and multiple RISs attached to a skyscrapers' high-rise facade). The sampling rate is set to $f_s = 50$ MHz. Similarly, the maximum delay spread of the k-th RIS-UE link is set to $L_{k,\text{RU}} = L_{k,\text{RU}}^{\text{zero}} + L_{k,\text{RU}}^{\text{non-zero}}$, $\forall k \in \mathcal{K}$ taps, where the first $L_{k,\text{RU}}^{\text{zero}} = \lfloor d_{k,\text{RU}} f_s / c \rceil$ taps characterize the transmission delay of the RIS-UE link associated with the k-th RIS, while the last $L_{k,\text{RU}}^{\text{non-zero}}$ taps characterize the k-th RIS-UE channel depending on the surrounding scatterers. Unless specified otherwise, we set $L_{k,\text{RU}}^{\text{non-zero}} = 5$ taps, where each non-zero NLoS tap is modeled by Rayleigh fading having a uniform power delay profile, i.e., $v_{k,m}(l) \sim \mathcal{CN}(0,1)$, $l = L_{k,\text{RU}}^{\text{zero}}, L_{k,\text{RU}}^{\text{zero}} + 1, \cdots, L_{k,\text{RU}} - 1$ [36]. The Rician factor of all RIS-UE links is set to $\zeta_{k,\text{RU}} = 3$ dB, $\forall k \in \mathcal{K}$. For the sake of normalization by the channel gain, the RIS-UE channels generated are then scaled by a coefficient of $1 / \sqrt{\zeta_{k,\text{RU}} + L_{k,\text{RU}}^{\text{non-zero}}}$.

Furthermore, for the LoS path, as the RIS array size is practically much smaller than the length of the BS-RIS and RIS-UE links, the channel gains of all links reflected via the same RIS are approximately identical, while their phases are correlated depending on the respective physical layout. The rays arriving at the k-th RIS are assumed to be parallel for all elements, with a common angle of arrival (AOA) composed of an elevation angle of $\varphi_{e,k,\text{BR}} = 0$ and an azimuth angle of $\varphi_{a,k,\text{BR}} = \arctan\left(k d_{\text{BR}-y} / d_{\text{BR}-x}\right)$, $\forall k \in \mathcal{K}$. Similarly, the rays reflected by the k-th RIS are of a common angle of departure (AOD) composed of an elevation angle of

$$\varphi_{e,k,\text{RU}} = -\arctan\left(d_{\text{R}-z} \Big/ \sqrt{(d_{\text{BU}-x} - d_{\text{BR}-x})^2 + \left(k d_{\text{BR}-y}\right)^2}\right)$$

and an azimuth angle of

$$\varphi_{a,k,\text{RU}} = \pi/2 + \arctan\left((d_{\text{BU}-x} - d_{\text{BR}-x}) / k d_{\text{BR}-y}\right)$$

. For an arbitrary one of the three RISs, let (m_x, m_z) denote the location of a RIS element, with $1 \le m_x \le M_x$ and $1 \le m_z \le M_z$. In the following simulations associated with varying M, we fix $M_x = 10$ and increase M_z linearly with $M = M_x M_z$. Let $\omega(m_x, m_z)$ denote the phase offset of the BS-RIS link at (m_x, m_z) with respect to that at $(1,1)$ (i.e., the one at the top left), thus we have

$$\begin{aligned}\omega_{k,\text{BR}}(m_x, m_z) = &\frac{2\pi}{\lambda}(m_x - 1)\, d \cos\varphi_{e,k,\text{BR}} \cos\varphi_{a,k,\text{BR}} \\ &+ \frac{2\pi}{\lambda}(m_z - 1)\, d \sin\varphi_{e,k,\text{BR}},\end{aligned} \tag{29}$$

where d denotes the RIS element spacing and λ denotes the carrier wavelength. In our simulations, we set $d = 0.05$ m and $\lambda = 0.33$ m corresponding to a carrier frequency of $f_c = 900$ MHz [62]. Similarly, the phase offset for the LoS path of the RIS-UE link $\omega_{k,\text{RU}}(m_x, m_z)$ can be obtained by substituting $\varphi_{e,k,\text{RU}}$ and $\varphi_{a,k,\text{RU}}$ into (29). As a result, the phase difference of the LoS paths for all the RIS elements in the BS-RIS link and RIS-UE link is fixed. Moreover, the path loss of the BS-RIS and RIS-UE links is modeled by $\rho_{k,\text{BR/RU}}^2 = C_0 d_{k,\text{BR/RU}}^{-\alpha_{k,\text{BR/RU}}}$, where $C_0 = -30$ dB is the power loss at the reference distance of $d = 1$ m, $d_{k,\text{BR}}$ and $d_{k,\text{RU}}$ denote the distance of the BS-RIS and the RIS-UE links, respectively, with respect to the k-th RIS; while $\alpha_{k,\text{BR}} = 2.2$ and $\alpha_{k,\text{RU}} = 2.8$ denote the corresponding path loss exponents, respectively, which are assumed to be the same for all RISs. Additionally, the number of OFDM subcarriers is set to $N = 1024$, while the CP length is thus set as $N_{CP} = 16$. In our simulations, we assume $\bar{\tau}_{\max} \ge N_{CP}$ in order to attain the best performance of adjustable-delay RIS, which corresponds to $\tau_{\max} \ge 0.32$ μs. The total transmit power at the BS is given by $P = 20$ dBm, while the average noise power is set to $\sigma^2 = -100$ dBm [43]. In order to characterize the maximum achievable rate, the SNR gap is set to $\Gamma = 0$ dB. The number of Gaussian randomization for solving Problem ($P4$-SDR) in Algorithm 1 is chosen as $Q = 100$, while the number of random initializations in Algorithm 1 is set to $J = 10$. All the results are averaged over 1,000 independent channel realizations.

B. Benchmark Schemes

Firstly, we assume that perfect CSI is available and ignore any pilot overhead required for CSI acquisition. The

achievable rate is thus computed using (8). For the sake of comparison, we consider the following 8 benchmark schemes upon considering two transmit power allocation schemes (i.e., equal solution and water-filling solution), two kinds of RIS elements (i.e., employing adjustable-delay RIS or not), and two phase shift configuration methods (i.e., statistical and optimal). More specifically, the 8 benchmark schemes are listed in Table II, where their respective operation setups are as follows:

1) Transmit power allocation

- Equal solution: Allocating an equal amount of power to all subcarriers;
- Water-filling solution: Performing the power allocation according to (11).

2) RIS elements

- Conventional RIS: Each reflecting element is capable of only adjusting the phase of the incident signals;
- Adjustable-delay RIS: Each reflecting element is capable of adjusting both the phase and delay of the incident signals.

3) Phase shift configuration method

- Statistical: Each RIS coefficient is configured by aligning the LOS components of the BS-RIS and RIS-UE links;
- Optimal: Each RIS coefficient is optimally configured based on (22) in Algorithm 2.

Note that for the adjustable-delay RIS elements, the statistical phase shift configuration method adjusts the RIS's delay by aligning it to the LoS path of each reflected channel, while the optimal phase shift configuration method adjusts the RIS's delay according to (22). In the following figures, we will use the abbreviations seen in Table II for representing each scheme, where the strongest-CIR maximization (SCM) method is proposed in [28] for conventional RIS-aided OFDM systems.

C. Performance Comparison with Benchmark Schemes

Fig. 5(a) depicts the achievable rate versus the horizontal BS-UE distance, where we consider $M_z = 1$. It can be observed from Fig. 5(a) that for the conventional RIS-assisted OFDM systems, the phase shift configuration based on the statistical CSI (i.e., the deterministic LoS path) and that based on the instantaneous CSI result in an improved rate. The optimal water-filling power allocation is capable of further increasing the achievable rate compared to its counterparts relying on the equal-power allocation solution. Moreover, adjustable-delay RIS is capable of substantially increasing the achievable rate beyond those operating with conventional RIS upon aligning the strongest taps of different reflected channels by adjusting the RIS delay. Explicitly, when the UE moves in the vicinity of the nearest RIS, i.e., $d_{\mathrm{BU}-x} = 100$ m, the employment of adjustable-delay RIS increases the achievable rate from 0.08 b/s/Hz to 0.135 b/s/Hz for the optimal phase shift configuration relying on the water-filling solution, which is a rate increase of about 70%. In summary, the RIS is capable of creating a hot spot by collecting energy diffused by the channel to improve the

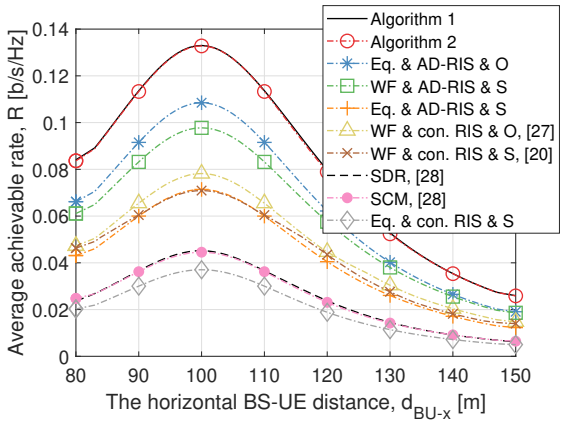

(a)

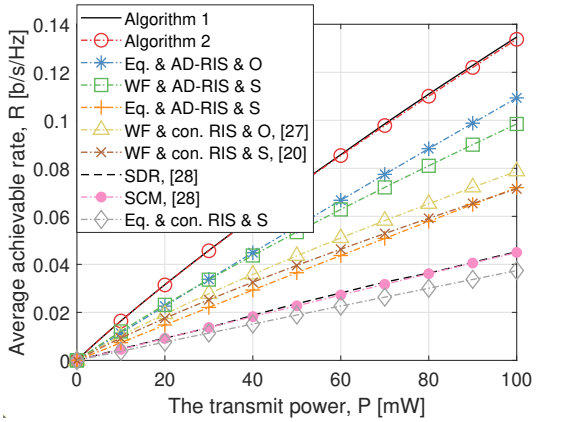

(b)

Fig. 5. Achievable rate versus (a) the horizontal BS-UE distance; (b) the total transmit power.

QoS of users in its vicinity. Furthermore, the adjustable-delay RIS introduced in this paper further improves the potential of RIS in wideband communications. Furthermore, the STA method (i.e., Algorithm 2) conceived approaches the performance of the high-quality sub-optimal Algorithm 1, despite its significantly reduced complexity. Similarly, the low-complexity SCM method achieves comparable performance to that of the SDR method designed for conventional RIS-aided OFDM systems.

In Fig. 5(b), we compare the achievable rate of the SDR-based AO method and of the benchmark schemes versus the transmit power at the BS, where we set $M_z = 1$ and $d_{\mathrm{BU}-x} = 100$ m. As expected, the achievable rate increases with the transmit power. More specifically, the SDR-based AO method and the STA method exhibit the fastest growth. The low-complexity STA method behaves competitively with respect to the SDR-based AO algorithm, exhibiting only a modest rate erosion of about 0.005 b/s/Hz. Compared to the conventional RIS-assisted OFDM systems relying on the optimal configuration, the employment of adjustable-delay RIS increases the achievable rate from 0.075 b/s/Hz to 0.13 b/s/Hz for $P = 100$ mW, maintaining a rate increase in excess of 70%, which benefits from the fact that the adjustable-delay RIS performs beamforming for all subcarriers, rather

than on the carrier frequency as in the conventional design. This significantly improves the beamforming efficiency. In addition, for the conventional RIS-assisted OFDM systems, the statistical phase shift configuration almost matches the optimal phase shift design, with only 0.01 b/s/Hz rate loss. By contrast, the adjustable-delay RIS exploits the instantaneous CSI more effectively, increasing the rate by about 0.04 b/s/Hz, regardless of whether the water-filling or the equal power allocation solution is used. This is also due to the fact that adjustable-delay RIS further improves the composite channel gain. In a nutshell, the setups employing adjustable-delay RIS outperform their conventional counterparts.

Fig. 6(a) compares the rate of different benchmark schemes versus the number of RIS elements. Recall from Figs. 5(b) that the proposed STA method incurs only marginal performance loss, despite its lower complexity than that of the SDR-based AO algorithm. Thus, we consider only the suboptimal STA method in the following in order to bypass the excessive computational burden of the SDR-based AO method for a large value of M. Observe from Fig. 6(a) that even the proposed adjustable-delay RIS-aided scheme adopting the equal power allocation solution outperforms all its conventional RIS-aided counterparts. Specifically, for the conventional RIS-assisted systems, the optimal phase shift configuration relying on the water-filling solution barely catches up with the statistical phase shift configuration employing adjustable-delay RIS. The equal-power allocation solution operating without adjustable-delay RIS results in poorer performance. Furthermore, note that as the number of elements increases, the advantages of the proposed design over its conventional RIS-aided counterparts will be gradually highlighted, which is because the adjustable-delay RIS is capable of collecting more power from the aligned taps for an increased number of RIS elements.

Fig. 6(b) portrays the achievable rate versus the number of OFDM subcarriers, where we set $M_z = 10$. Observe from Fig. 6(b) that the achievable rate decreases upon increasing the number of subcarriers, which potentially implies that the RIS attains higher performance gains for narrowband signals. This raises the question of whether to adopt single-carrier or multi-carrier transmission for future large-scale RIS deployments. Nevertheless, the employment of adjustable-delay RIS always brings about significant performance improvements, regardless of adopting the optimal phase shift configuration relying on instantaneous CSI or the suboptimal phase shift configuration relying on statistical CSI. By contrast, the statistical RIS configuration operating without adjustable-delay RIS performs similarly to its optimal RIS configuration-based counterparts, both of which suffer however from a rate loss of about 0.55 b/s/Hz compared to the proposed design, when considering OFDM systems having $N = 16$ subcarriers.

Fig. 7(a) evaluates the effects of the CIR length on the achievable rate upon adjusting the number of non-zero taps of the RIS-UE links. It can be observed that as the channel gain disperses in the delay domain, it is impossible to align all power components to the desired taps. As a result, the achievable rate decreases as the CIR length increases, bearing in mind that we are considering the normalized channel gain.

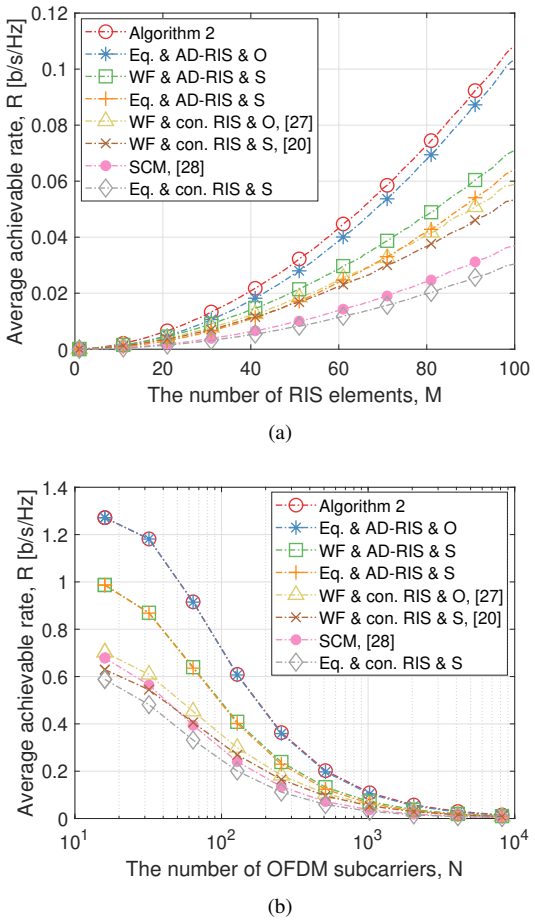

Fig. 6. Achievable rate versus (a) the number of RIS elements; (b) the number of OFDM subcarriers.

Additionally, when considering a single non-zero tap of the RIS-UE link, the end-to-end OFDM channel relying on the conventional RIS remains a frequency-selective channel due to the diverse delays caused by distributed RISs. By contrast, the adjustable-delay RIS converts the end-to-end channel into a frequency-flat channel by aligning all taps in the delay domain. Thus the equal power allocation solution shares the optimal performance with the water-filling solution. With the increase in the number of channel taps, the water-filling solution exhibits a slight performance improvement compared to the equal power allocation solution. In all setups considered in Fig. 7(a), the optimal configuration relying on adjustable-delay RIS maintains the optimal performance, followed by its counterpart relying on statistical RIS configuration. The latter still outperforms the optimal configuration operating with conventional RIS by about 0.02 b/s/Hz. The optimal configuration relying on adjustable-delay RIS attains about twice the achievable rate of that relying on conventional RIS.

Fig. 7(b) shows the achievable rate versus the Rician factor of the RIS-UE link. It can be seen that the achievable rate increases with the Rician factor due to the fact that more power is concentrated on the deterministic LoS path for a high Rician factor. Hence, the channels reflected via different RIS

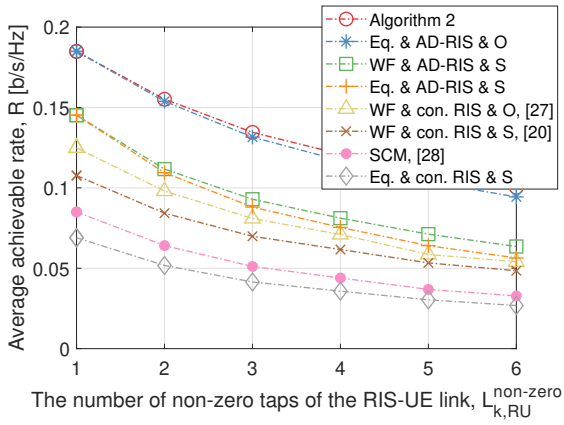

(a)

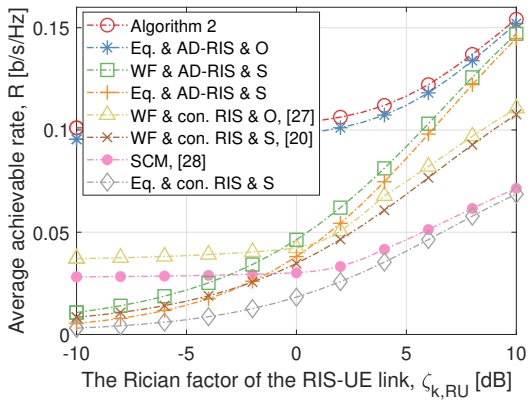

(b)

Fig. 7. Achievable rate versus (a) the number of non-zero taps of the RIS-UE link; (b) the Rician factor.

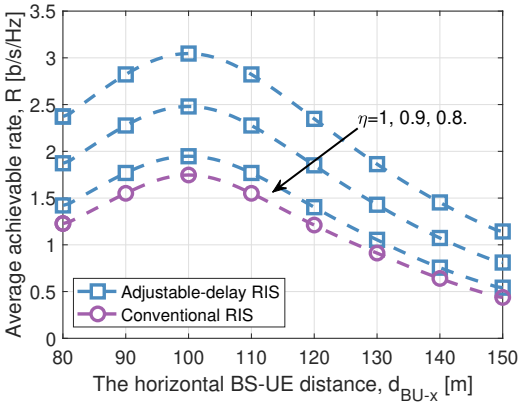

(a)

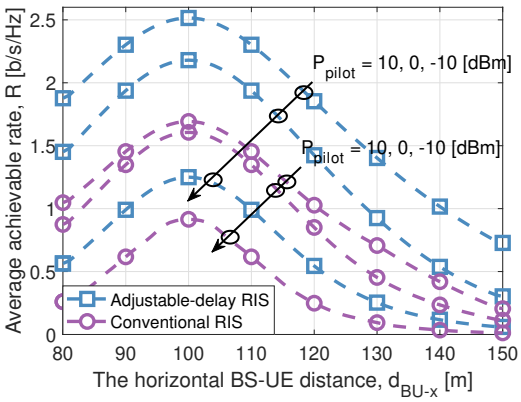

(b)

Fig. 8. (a) Achievable rate versus the horizontal BS-UE distance, where the practical adjustable-delay RIS component's power decay is considered. (b) Achievable rate versus the horizontal BS-UE distance, where the channel estimation errors are considered. The decay factor is set to $\eta = 0.9$.

elements are more likely to be constructively superimposed on all subcarriers for improving the average achievable rate. Specifically, for a low Rician factor, the RIS configuration relying on statistical CSI suffers from a severe performance penalty compared to the optimal configuration relying on instantaneous CSI. With the increase of the Rician factor, the gap between the statistical RIS configuration and the optimal RIS configuration will be progressively narrowed, because a high Rician factor generally results in all reflected channels being of a single tap and thus coherently superimposed on all subcarriers, even when relying on only the statistical rather accurate CSI (i.e., ***Lemma 1***). It shows that for the RIS-UE link having a strong LoS component associated with few local scatterers, even the statistical CSI is adequate for performing the RIS configuration without causing substantial performance loss. Additionally, the proposed design attains the best performance among all setups considered. For example, when the Rician factor is $\zeta_{k,\mathrm{RU}} = 0$ dB, the achievable rate of the proposed design is more than twice that without employing adjustable-delay RIS. Upon further increasing the Rician factor to $\zeta_{k,\mathrm{RU}} = 10$ dB, the proposed design still has a rate advantage of 0.04 b/s/Hz.

D. Impact of Hardware Imperfections

Next, we consider the effect of the practical adjustable-delay RIS component's power decay versus delay on the proposed scheme. We assume an exponentially decaying model to characterize the power decay profile caused by the practical adjustable-delay RIS component [54], which is expressed as $p_{\mathrm{decay}} = \eta^{\bar{\tau}}$, where $0 < \eta \leq 1$ and $\bar{\tau}$ denote the decay factor and delay, respectively. Fig. 8(a) shows the achievable rate of the proposed scheme considering the power distortion caused by adjustable delay, where we set $M = 100$, $C_0 = -20$ dB, and $f_s = 10$ MHz. For the sake of illustration, we only consider the optimal setup in the presence/absence of adjustable-delay RIS. As observed from Fig. 8(a), upon increasing the decay factor, the performance of the proposed scheme is degraded due to the power attenuation incurred by the practical adjustable-delay RIS component. Nevertheless, the proposed scheme still retains a performance improvement of about 0.2 b/s/Hz for $\eta = 0.8$, which implies that, for a moderate decay factor, the performance gain attained by aligning the strongest taps outweighs the penalty caused by the power attenuation introduced by RIS delay. It is worth noting that the RIS's delay for all setups in Fig. 8(a) is configured according to

(22), which implies that the achievable rate in the presence of power decay can be further improved upon jointly considering the RIS's delay and the power decay. As a result, there exists a fundamental tradeoff between the adjustable-delay RIS's delay and the decay factor.

Finally, Fig. 8(b) evaluates the effects of channel estimation errors, where we consider the uplink pilot power of $P_{\text{pilot}} = 10,\ 0,\ -10$ dBm, respectively. Moreover, the average noise power at the BS is set to $\sigma_{\text{BS}}^2 = -110$ dBm and the power decay factor of the practical adjustable-delay RIS component is set to $\eta = 0.9$. The DFT-based reflection pattern is employed for minimizing the channel estimates' MSE [33]. Interested readers are referred to [27] for further details on the channel estimation for RIS-assisted OFDM systems. As seen from Fig. 8(b), the channel estimation errors degrade the achievable rate of both the proposed scheme employing adjustable-delay RIS and of the conventional scheme dispensing with our adjustable-delay RIS due to the passive beamformer's performance erosion imposed by the imperfect CSI. Hence, multiple reflection channels cannot be perfectly aligned. Nevertheless, the proposed scheme always outperforms the traditional scheme under the same setup thanks to the adjustable-delay RIS introduced. In particular, considering the practical adjustable-delay RIS component's power decay of $\eta = 0.9$ and the imperfect CSI of $P_{\text{pilot}} = -10$ dBm, the proposed scheme increases the achievable rate from 0.9 b/s/Hz to 1.25 b/s/Hz, with a rate improvement of about 40%. Note that the estimation overhead is proportional to the number of RIS elements, hence it is crucial to design an appropriate channel estimation scheme having a moderate overhead for practical deployment of RISs. One may refer to the element-grouping method of [28] and the codebook scheme of [42] for striking favorable tradeoffs between the overhead and the achievable rate.

VII. Conclusions

The adjustable-delay RIS philosophy relying on varactor diodes was proposed, which is capable of storing and retrieving the impinging waves, thus imposing an extra delay on the incident signals upon adjusting its EIT properties. Thanks to this new design DoF, adjustable-delay RIS is more likely to beneficially align multiple reflected channels on all subcarriers concurrently. Following this, we formulated a rate maximization problem of the RIS-assisted OFDM systems by jointly optimizing the transmit power and the RIS reflection coefficients as well as RIS delays. Furthermore, we proposed an SDR-based AO algorithm for finding a high-quality approximate solution for the non-convex problem formulated and conceived a low-complexity STA method upon aligning the strongest taps of all reflected channels. Finally, our simulations verify the advantages of the proposed algorithms over their traditional counterparts. In particular, the proposed algorithm outperforms the conventional schemes by up to 70% in terms of its rate improvement. Even after taking into account practical power decay coefficients and channel estimation errors, the proposed scheme attains a rate improvement of 40%. In summary, the proposed algorithm significantly improves the RIS's performance for wideband signals and it is expected to mitigate the beam squint effect if extended to MIMO systems [63].

References

[1] E. G. Larsson, O. Edfors, F. Tufvesson, and T. L. Marzetta, "Massive MIMO for next generation wireless systems," *IEEE Commun. Mag.*, vol. 52, pp. 186–195, Feb. 2014.

[2] I. A. Hemadeh, K. Satyanarayana, M. El-Hajjar, and L. Hanzo, "Millimeter-wave communications: Physical channel models, design considerations, antenna constructions, and link-budget," *IEEE Commun. Surveys Tuts.*, vol. 20, pp. 870–913, 2nd Quarter 2018.

[3] J. G. Andrews, "Seven ways that hetnets are a cellular paradigm shift," *IEEE Commun. Mag.*, vol. 51, pp. 136–144, Mar. 2013.

[4] N. Bonello, S. Chen, and L. Hanzo, "Low-density parity-check codes and their rateless relatives," *IEEE Commun. Surveys Tuts.*, vol. 13, pp. 3–26, Jan. 2011.

[5] X. You *et al.*, "Towards 6G wireless communication networks: vision, enabling technologies, and new paradigm shifts," *Sci. China Inf. Sci.*, vol. 64, pp. 335–349, Nov. 2020.

[6] S. Yang and L. Hanzo, "Fifty years of MIMO detection: The road to large-scale MIMOs," *IEEE Commun. Surveys Tuts.*, vol. 17, pp. 1941–1988, 4th Quarter 2015.

[7] W. Saad, M. Bennis, and M. Chen, "A vision of 6G wireless systems: Applications, trends, technologies, and open research problems," *IEEE Netw.*, vol. 34, pp. 134–142, May. 2020.

[8] K. B. Letaief, W. Chen, Y. Shi, J. Zhang, and Y.-J. A. Zhang, "The roadmap to 6G: AI empowered wireless networks," *IEEE Commun. Mag.*, vol. 57, pp. 84–90, Aug. 2019.

[9] J. An, C. Xu, Q. Wu, D. W. K. Ng, M. D. Renzo, C. Yuen, and L. Hanzo, "Codebook-based solutions for reconfigurable intelligent surfaces and their open challenges," *IEEE Wireless Commun.*, pp. 1–8, Early Access, 2022.

[10] Q. Wu and R. Zhang, "Intelligent reflecting surface enhanced wireless network via joint active and passive beamforming," *IEEE Trans. Wireless Commun.*, vol. 18, pp. 5394–5409, Nov. 2019.

[11] C. Huang, S. Hu, G. C. Alexandropoulos, A. Zappone, C. Yuen, R. Zhang, M. D. Renzo, and M. Debbah, "Holographic MIMO surfaces for 6G wireless networks: Opportunities, challenges, and trends," *IEEE Wireless Commun.*, vol. 27, pp. 118–125, Oct. 2020.

[12] M. Di Renzo, A. Zappone, M. Debbah, M.-S. Alouini, C. Yuen, J. de Rosny, and S. Tretyakov, "Smart radio environments empowered by reconfigurable intelligent surfaces: How it works, state of research, and the road ahead," *IEEE J. Sel. Areas Commun.*, vol. 38, pp. 2450–2525, Nov. 2020.

[13] Q. Wu, S. Zhang, B. Zheng, C. You, and R. Zhang, "Intelligent reflecting surface-aided wireless communications: A tutorial," *IEEE Trans. Commun.*, vol. 69, pp. 3313–3351, May. 2021.

[14] L. Dai, B. Wang, M. Wang, X. Yang, J. Tan, S. Bi, S. Xu, F. Yang, Z. Chen, M. D. Renzo, C.-B. Chae, and L. Hanzo, "Reconfigurable intelligent surface-based wireless communications: Antenna design, prototyping, and experimental results," *IEEE Access*, vol. 8, pp. 45913–45923, Mar. 2020.

[15] C. Huang, A. Zappone, G. C. Alexandropoulos, M. Debbah, and C. Yuen, "Reconfigurable intelligent surfaces for energy efficiency in wireless communication," *IEEE Trans. Wireless Commun.*, vol. 18, pp. 4157–4170, Aug. 2019.

[16] C. Xu, J. An, T. Bai, L. Xiang, S. Sugiura, R. G. Maunder, L.-L. Yang, and L. Hanzo, "Reconfigurable intelligent surface assisted multi-carrier wireless systems for doubly selective high-mobility Ricean channels," *IEEE Trans. Veh. Technol.*, vol. 71, pp. 4023–4041, Apr. 2022.

[17] E. Bjornson, O. Ozdogan, and E. G. Larsson, "Intelligent reflecting surface versus decode-and-forward: How large surfaces are needed to beat relaying?," *IEEE Wireless Commun. Lett.*, vol. 9, pp. 244–248, Feb. 2020.

[18] J. Zhang, E. Björnson, M. Matthaiou, D. W. K. Ng, H. Yang, and D. J. Love, "Prospective multiple antenna technologies for beyond 5G," *IEEE J. Sel. Areas Commun.*, vol. 38, pp. 1637–1660, Aug. 2020.

[19] J. An, C. Xu, L. Gan, and L. Hanzo, "Low-complexity channel estimation and passive beamforming for RIS-assisted MIMO systems relying on discrete phase shifts," *IEEE Trans. Commun.*, vol. 70, pp. 1245–1260, Feb. 2022.

[20] Y. Han, W. Tang, S. Jin, C.-K. Wen, and X. Ma, "Large intelligent surface-assisted wireless communication exploiting statistical CSI," *IEEE Trans. Veh. Technol.*, vol. 68, pp. 8238–8242, Aug. 2019.

[21] M. Cui, G. Zhang, and R. Zhang, "Secure wireless communication via intelligent reflecting surface," *IEEE Wireless Commun. Lett.*, vol. 8, pp. 1410–1414, May. 2019.

[22] C. Pan, H. Ren, K. Wang, W. Xu, M. Elkashlan, A. Nallanathan, and L. Hanzo, "Multicell MIMO communications relying on intelligent reflecting surfaces," *IEEE Trans. Wireless Commun.*, vol. 19, pp. 5218–5233, Aug. 2020.

[23] H. Guo, Y.-C. Liang, J. Chen, and E. G. Larsson, "Weighted sum-rate maximization for reconfigurable intelligent surface aided wireless networks," *IEEE Trans. Wireless Commun.*, vol. 19, pp. 3064–3076, May. 2020.

[24] S. Zhang and R. Zhang, "Capacity characterization for intelligent reflecting surface aided MIMO communication," *IEEE J. Sel. Areas Commun.*, vol. 38, pp. 1823–1838, Aug. 2020.

[25] B. Di, H. Zhang, L. Song, Y. Li, Z. Han, and H. V. Poor, "Hybrid beamforming for reconfigurable intelligent surface based multi-user communications: Achievable rates with limited discrete phase shifts," *IEEE J. Sel. Areas Commun.*, vol. 38, pp. 1809–1822, Aug. 2020.

[26] S. Abeywickrama, R. Zhang, Q. Wu, and C. Yuen, "Intelligent reflecting surface: Practical phase shift model and beamforming optimization," *IEEE Trans. Commun.*, vol. 68, pp. 5849–5863, Sept. 2020.

[27] Y. Yang, B. Zheng, S. Zhang, and R. Zhang, "Intelligent reflecting surface meets OFDM: Protocol design and rate maximization," *IEEE Trans. Commun.*, vol. 68, pp. 4522–4535, Jul. 2020.

[28] B. Zheng and R. Zhang, "Intelligent reflecting surface-enhanced OFDM: Channel estimation and reflection optimization," *IEEE Wireless Commun. Lett.*, vol. 9, pp. 518–522, Apr. 2020.

[29] Y. Han, S. Zhang, L. Duan, and R. Zhang, "Cooperative double-IRS aided communication: Beamforming design and power scaling," *IEEE Wireless Commun. Lett.*, vol. 9, pp. 1206–1210, Aug. 2020.

[30] C. Xu, J. An, T. Bai, S. Sugiura, R. G. Maunder, L.-L. Yang, M. Di Renzo, and L. Hanzo, "Antenna selection for reconfigurable intelligent surfaces: A transceiver-agnostic passive beamforming configuration," *IEEE Trans. Wireless Commun.*, vol. 22, pp. 7756–7774, Nov. 2023.

[31] C. Xu, J. An, T. Bai, S. Sugiura, R. G. Maunder, Z. Wang, L.-L. Yang, and L. Hanzo, "Channel estimation for reconfigurable intelligent surface assisted high-mobility wireless systems," *IEEE Trans. Veh. Technol.*, vol. 72, pp. 718–734, Jan. 2023.

[32] J. An, L. Wang, C. Xu, L. Gan, and L. Hanzo, "Optimal pilot power based channel estimation improves the throughput of intelligent reflective surface assisted systems," *IEEE Trans. Veh. Technol.*, vol. 69, pp. 16202–16206, Dec. 2020.

[33] T. L. Jensen and E. De Carvalho, "An optimal channel estimation scheme for intelligent reflecting surfaces based on a minimum variance unbiased estimator," in *Proc. IEEE Int. Conf. Acoust., Speech Signal Process. (ICASSP)*, pp. 5000–5004, May. 2020.

[34] C. You, B. Zheng, and R. Zhang, "Channel estimation and passive beamforming for intelligent reflecting surface: Discrete phase shift and progressive refinement," *IEEE J. Sel. Areas Commun.*, vol. 38, pp. 2604–2620, Nov. 2020.

[35] Z. Wang, L. Liu, and S. Cui, "Channel estimation for intelligent reflecting surface assisted multiuser communications: Framework, algorithms, and analysis," *IEEE Trans. Wireless Commun.*, vol. 19, pp. 6607–6620, Oct. 2020.

[36] J. An, Q. Wu, and C. Yuen, "Scalable channel estimation and reflection optimization for reconfigurable intelligent surface-enhanced OFDM systems," *IEEE Wireless Commun. Lett.*, vol. 11, pp. 796–800, Apr. 2022.

[37] J. Yao, J. Xu, W. Xu, C. Yuen, and X. You, "A universal framework of superimposed RIS-phase modulation for MISO communication," *IEEE Trans. Veh. Technol.*, vol. 72, pp. 5413–5418, Apr. 2023.

[38] J. An, C. Yuen, C. Xu, H. Li, D. W. K. Ng, M. Di Renzo, M. Debbah, and L. Hanzo, "Stacked intelligent metasurface-aided MIMO transceiver design," *arXiv preprint arXiv:2311.09814*, 2023.

[39] X. Yu, D. Xu, Y. Sun, D. W. K. Ng, and R. Schober, "Robust and secure wireless communications via intelligent reflecting surfaces," *IEEE J. Sel. Areas Commun.*, vol. 38, pp. 2637–2652, Nov. 2020.

[40] C. Pan, H. Ren, K. Wang, M. Elkashlan, A. Nallanathan, J. Wang, and L. Hanzo, "Intelligent reflecting surface aided MIMO broadcasting for simultaneous wireless information and power transfer," *IEEE J. Sel. Areas Commun.*, vol. 38, pp. 1719–1734, Aug. 2020.

[41] W. Xu, J. An, C. Huang, L. Gan, and C. Yuen, "Deep reinforcement learning based on location-aware imitation environment for RIS-aided mmwave MIMO systems," *IEEE Wireless Commun. Lett.*, vol. 11, pp. 1493–1497, Jul. 2022.

[42] J. An and L. Gan, "The low-complexity design and optimal training overhead for IRS-assisted MISO systems," *IEEE Wireless Commun. Lett.*, vol. 10, pp. 1820–1824, Aug. 2021.

[43] J. An, C. Xu, L. Wang, Y. Liu, L. Gan, and L. Hanzo, "Joint training of the superimposed direct and reflected links in reconfigurable intelligent surface assisted multiuser communications," *IEEE Trans. Green Commun. Netw.*, vol. 6, pp. 739–754, Jun. 2022.

[44] X. Li, Y. Zheng, M. Zeng, Y. Liu, and O. A. Dobre, "Enhancing secrecy performance for STAR-RIS NOMA networks," *IEEE Trans. Veh. Technol.*, vol. 72, pp. 2684–2688, Feb. 2023.

[45] S. Li, B. Duo, X. Yuan, Y.-C. Liang, and M. Di Renzo, "Reconfigurable intelligent surface assisted UAV communication: Joint trajectory design and passive beamforming," *IEEE Wireless Commun. Lett.*, vol. 9, pp. 716–720, May. 2020.

[46] T. Bai, C. Pan, H. Ren, Y. Deng, M. Elkashlan, and A. Nallanathan, "Resource allocation for intelligent reflecting surface aided wireless powered mobile edge computing in OFDM systems," *IEEE Trans. Wireless Commun.*, vol. 20, pp. 5389–5407, Aug. 2021.

[47] J. An, C. Xu, D. W. K. Ng, G. C. Alexandropoulos, C. Huang, C. Yuen, and L. Hanzo, "Stacked intelligent metasurfaces for efficient holographic MIMO communications in 6G," *IEEE J. Sel. Areas Commun.*, vol. 41, pp. 2380–2396, Aug. 2023.

[48] J. An, C. Yuen, C. Huang, M. Debbah, H. Vincent Poor, and L. Hanzo, "A tutorial on holographic MIMO communications—part I: Channel modeling and channel estimation," *IEEE Commun. Lett.*, vol. 27, pp. 1664–1668, Jul. 2023.

[49] A. M. Elbir, A. Papazafeiropoulos, P. Kourtessis, and S. Chatzinotas, "Deep channel learning for large intelligent surfaces aided mm-wave massive MIMO systems," *IEEE Wireless Commun. Lett.*, vol. 9, pp. 1447–1451, Sept. 2020.

[50] S. Lin, B. Zheng, G. C. Alexandropoulos, M. Wen, F. Chen, and S. Mumtaz, "Adaptive transmission for reconfigurable intelligent surface-assisted OFDM wireless communications," *IEEE J. Sel. Areas Commun.*, vol. 38, pp. 2653–2665, Nov. 2020.

[51] B. Zheng, C. You, and R. Zhang, "Intelligent reflecting surface assisted multi-user OFDMA: Channel estimation and training design," *IEEE Trans. Wireless Commun.*, vol. 19, pp. 8315–8329, Dec. 2020.

[52] Z. Zhang and L. Dai, "A joint precoding framework for wideband reconfigurable intelligent surface-aided cell-free network," *IEEE Trans. Signal Process.*, Early Access, 2021.

[53] Z. He, H. Shen, W. Xu, and C. Zhao, "Low-cost passive beamforming for RIS-aided wideband OFDM systems," *IEEE Wireless Commun. Lett.*, vol. 11, pp. 318–322, Feb. 2022.

[54] T. Nakanishia and M. Kitano, "Storage and retrieval of electromagnetic waves using electromagnetically induced transparency in a nonlinear metamaterial," *Appl. Phys. Lett.*, vol. 112, pp. 1–5, May. 2018.

[55] T. Nakanishi, T. Otani, Y. Tamayama, and M. Kitano, "Storage of electromagnetic waves in a metamaterial that mimics electromagnetically induced transparency," *Phys. Rev. B*, vol. 87, p. 161110, Apr. 2013.

[56] Z. Bai, D. Xu, and G. Huang, "Storage and retrieval of electromagnetic waves with orbital angular momentum via plasmon-induced transparency," *Optics Express*, vol. 25, pp. 785–798, Jan. 2017.

[57] Y. Cheng, W. Peng, and T. Jiang, "Self-sustainable RIS aided wireless power transfer scheme," *IEEE Trans. Veh. Technol.*, vol. 72, pp. 881–892, Jan. 2023.

[58] T. Nakanishi, T. Otani, Y. Tamayama, and M. Kitano, "Storage of electromagnetic waves in a metamaterial that mimics electromagnetically induced transparency," *Phys. Rev. B*, vol. 87, p. 161110, Apr. 2013.

[59] X. Yu, V. Jamali, D. Xu, D. W. K. Ng, and R. Schober, "Smart and reconfigurable wireless communications: From IRS modeling to algorithm design," *IEEE Wireless Commun.*, vol. 28, pp. 118–125, Dec. 2021.

[60] M. Grant and S. Boyd, "CVX: Matlab software for disciplined convex programming, version 2.1." http://cvxr.com/cvx, Mar. 2014.

[61] D. C. Montgomery and G. C. Runger, *Applied Statistics and Probability for Engineers*. Hoboken, NJ, USA: Wiley, 2011.

[62] W. Tang, M. Z. Chen, X. Chen, J. Y. Dai, Y. Han, M. Di Renzo, Y. Zeng, S. Jin, Q. Cheng, and T. J. Cui, "Wireless communications with reconfigurable intelligent surface: Path loss modeling and experimental measurement," *IEEE Trans. Wireless Commun.*, vol. 20, pp. 421–439, Jan. 2021.

[63] Y. Chen, Y. Xiong, D. Chen, T. Jiang, S. X. Ng, and L. Hanzo, "Hybrid precoding for wideband millimeter wave MIMO systems in the face of beam squint," *IEEE Trans. Wireless Commun.*, vol. 20, pp. 1847–1860, Mar. 2021.

Jiancheng An received the B.S. degree in Electronics and Information Engineering and the Ph.D. degree in Information and Communication Engineering from the University of Electronic Science and Technology of China (UESTC), Chengdu, China, in 2016 and 2021, respectively. From 2019 to 2020, he was a Visiting Scholar with the Next-Generation Wireless Group, University of Southampton, U.K. From 2021 to 2023, he was with the Engineering Product Development (EPD) Pillar, Singapore University of Technology and Design. He is currently a research fellow with the School of Electrical and Electronics Engineering, Nanyang Technological University (NTU), Singapore. His research interests include stacked intelligent metasurfaces (SIM), wave-based computing, and near-field communications.

Chao Xu (S'09-M'14-SM'19) received a B.Eng. degree from Beijing University of Posts and Telecommunications, China, and a BSc(Eng) with First Class Honours from Queen Mary, University of London, UK, through a Sino-UK joint degree program in 2008, both in Telecommunications. He obtained a MSc degree with distinction in Radio Frequency Communication Systems and a Ph.D. degree in Wireless Communications from the University of Southampton, UK in 2009 and 2015, respectively. He is currently a senior research fellow working at Next Generation Wireless Research Group, University of Southampton, UK. His research interests include index modulation, reconfigurable intelligent surfaces, noncoherent detection and turbo detection. He was awarded the Best M.Sc. Student in Broadband and Mobile Communication Networks by the IEEE Communications Society (United Kingdom and Republic of Ireland Chapter) in 2009. He also received 2012 Chinese Government Award for Outstanding Self-Financed Student Abroad and 2017 Dean's Award, Faculty of Physical Sciences and Engineering, the University of Southampton.

Derrick Wing Kwan Ng (S'06-M'12-SM'17-F'21) received his bachelor's degree (with first-class Honors) and the Master of Philosophy degree in electronic engineering from The Hong Kong University of Science and Technology (HKUST), Hong Kong, in 2006 and 2008, respectively, and his Ph.D. degree from The University of British Columbia, Vancouver, BC, Canada, in November 2012. He was a senior postdoctoral fellow at the Institute for Digital Communications, Friedrich-Alexander-University Erlangen-Nürnberg (FAU), Germany. He is currently a Scientia Associate Professor with the University of New South Wales, Sydney, NSW, Australia. His research interests include global optimization, physical layer security, IRS-assisted communication, UAV-assisted communication, wireless information and power transfer, and green (energy-efficient) wireless communications.

Since 2018, he has been listed as a Highly Cited Researcher by Clarivate Analytics (Web of Science). He was the recipient of the Australian Research Council (ARC) Discovery Early Career Researcher Award 2017, IEEE Communications Society Leonard G. Abraham Prize 2023, IEEE Communications Society Stephen O. Rice Prize 2022, Best Paper Awards at the WCSP 2020, 2021, IEEE TCGCC Best Journal Paper Award 2018, INISCOM 2018, IEEE International Conference on Communications (ICC) 2018, 2021, 2023, IEEE International Conference on Computing, Networking and Communications (ICNC) 2016, IEEE Wireless Communications and Networking Conference (WCNC) 2012, IEEE Global Telecommunication Conference (Globecom) 2011, 2021, and IEEE Third International Conference on Communications and Networking in China 2008. From January 2012 to December 2019, he served as an Editorial Assistant to the Editor-in-Chief of the IEEE Transactions on Communications. He is also the Editor of the IEEE Transactions on Communications and an Associate Editor-in-Chief for the IEEE Open Journal of the Communications Society.

Chau Yuen (S'02-M'06-SM'12-F'21) received the B.Eng. and Ph.D. degrees from Nanyang Technological University, Singapore, in 2000 and 2004, respectively. He was a Post-Doctoral Fellow with Lucent Technologies Bell Labs, Murray Hill, in 2005, and a Visiting Assistant Professor with The Hong Kong Polytechnic University in 2008. From 2006 to 2010, he was with the Institute for Infocomm Research, Singapore. From 2010 to 2023, he was with the Engineering Product Development Pillar, Singapore University of Technology and Design. Since 2023, he has been with the School of Electrical and Electronic Engineering, Nanyang Technological University.

Dr. Yuen received IEEE Communications Society Fred W. Ellersick Prize (2023), IEEE Marconi Prize Paper Award in Wireless Communications (2021), and EURASIP Best Paper Award for JOURNAL ON WIRELESS COMMUNICATIONS AND NETWORKING (2021). He was a recipient of the Lee Kuan Yew Gold Medal, the Institution of Electrical Engineers Book Prize, the Institute of Engineering of Singapore Gold Medal, the Merck Sharp and Dohme Gold Medal, and twice a recipient of the Hewlett Packard Prize. He received the IEEE Asia Pacific Outstanding Young Researcher Award in 2012 and IEEE VTS Singapore Chapter Outstanding Service Award on 2019.

Dr Yuen current serves as an Editor-in-Chief for Springer Nature Computer Science, Editor for IEEE TRANSACTIONS ON VEHICULAR TECHNOLOGY, IEEE SYSTEM JOURNAL, and IEEE TRANSACTIONS ON NETWORK SCIENCE AND ENGINEERING, where he was awarded as IEEE TNSE Excellent Editor Award and Top Associate Editor for TVT from 2009 to 2015. He also served as the guest editor for several special issues, including IEEE JOURNAL ON SELECTED AREAS IN COMMUNICATIONS, IEEE WIRELESS COMMUNICATIONS MAGAZINE, IEEE COMMUNICATIONS MAGAZINE, IEEE VEHICULAR TECHNOLOGY MAGAZINE, IEEE TRANSACTIONS ON COGNITIVE COMMUNICATIONS AND NETWORKING, and ELSEVIER APPLIED ENERGY.

He is a Distinguished Lecturer of IEEE Vehicular Technology Society, Top 2% Scientists by Stanford University, and also a Highly Cited Researcher by Clarivate Web of Science. He has 3 US patents and published over 500 research papers at international journals or conferences.

Lajos Hanzo (Life Fellow, IEEE) received Honorary Doctorates from the Technical University of Budapest and Edinburgh University. He is a Foreign Member of the Hungarian Science-Academy, Fellow of the Royal Academy of Engineering (FREng), of the IET, of EURASIP and holds the IEEE Eric Sumner Technical Field Award.